Supplementary information for

Carbene catalyzed synthesis of fluorophosphate cathode

Qingfeng Fu[a ‡], Wang Zhou[a ‡], Peng Gao[a ‡], Hongliang Dong[b,c], Shi Chen[d], Changling Fan[a,*], Jilei Liu[a,*]

[a] *College of Materials Science and Engineering, Hunan Joint International Laboratory of Advanced Materials and Technology for Clean Energy, Hunan Province Key Laboratory for Advanced Carbon Materials and Applied Technology, Hunan University, Changsha 410082, China*

[b] *Center for High Pressure Science and Technology Advanced Research, Pudong, Shanghai 201203, China*
[c] *State Key Laboratory of High Performance Ceramics and Superfine Microstructure, Shanghai Institute of Ceramics, Chinese Academy of Sciences, Shanghai 201899, China*
[d] *Joint Key Laboratory of the Ministry of Education, Institute of Applied Physics and Materials Engineering, University of Macau, Macau, 999078 China*

Corresponding author. E-mail address: liujilei@hnu.edu.cn (Jilei Liu); fancl@hnu.edu.cn.
[‡] Qingfeng Fu, Wang Zhou and Peng Gao contributed equally to this work.

The PDF file includes:

Supplementary Text
Figs. S1 to S52
Tables S1 to S4
References

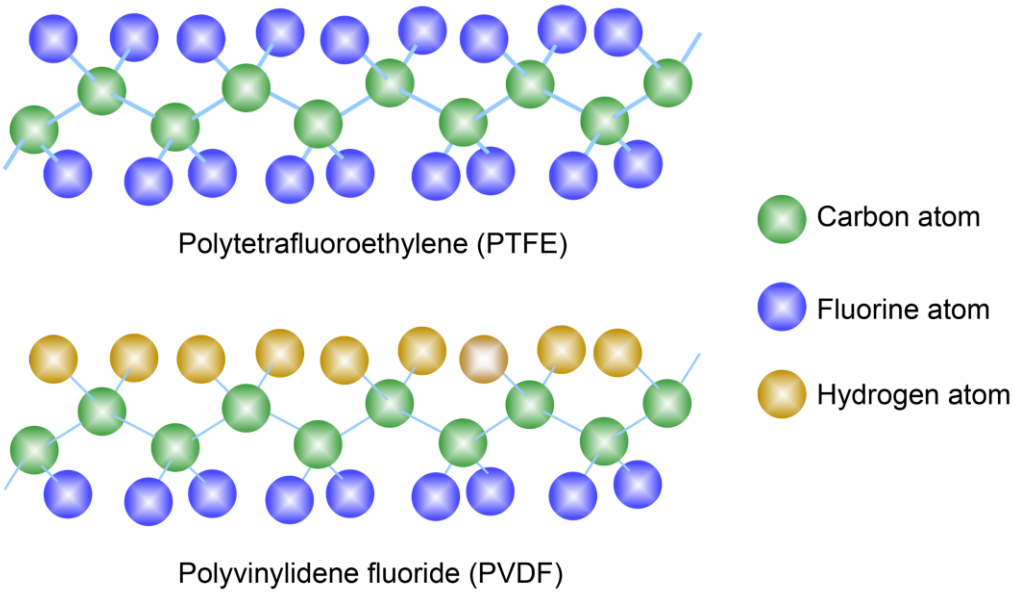

Fig. S1. Chemical molecular formula and abbreviation of polytetrafluoroethylene (PTFE) and polyvinylidene fluoride (PVDF).

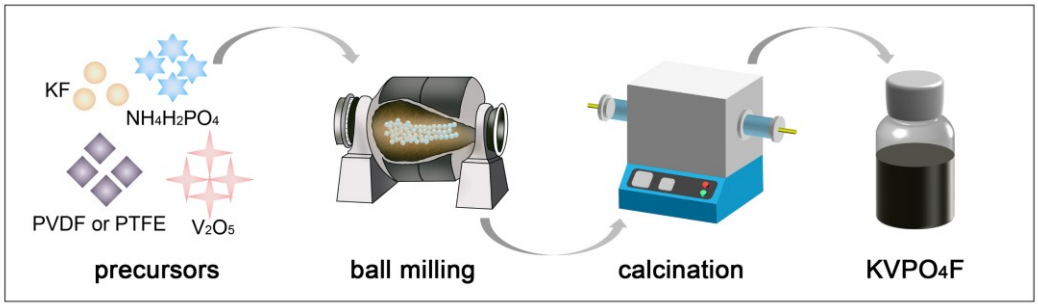

Fig. S2. Process for the preparation of $KVPO_4F$ using a scalable one-step solid-state reaction process.

Supplementary Note 1:

The influences of different amount PVDF/PTFE on phase purity of as-prepared samples were also investigated by using a series of structural and spectroscopic characterization techniques. The photo images of as-prepared samples with addition of different amount PVDF/PTFE are shown in **Fig. S3**. No solid particles were formed after calcination without PVDF/PTFE addition, which is likely due to the volatilization of V_2O_5 at temperatures higher than 700 °C.[1] It is noteworthy that the V_2O_5 is easy to volatilize when calcined at higher temperatures because of its low melting point and high saturated vapor pressure. The only way to prevent the volatilization of V_2O_5 is to reduce it to VO_2 or V_2O_3.[1] Therefore, the success of one-step solid-phase sintering process requires the use of reducing agents during the synthesis. The XRD patterns of as-synthesized samples calcined at 750 ºC with different adding amounts of PVDF/PTFE are shown in **Fig. S4a** and **Fig. S4b**. The unknown impurities are present with 5wt% adding amounts of both PVDF and PTFE despite their different peak positions, which is likely due to their different reaction pathways. After increasing the amount of PVDF/PTFE to 15wt% and 25wt%, the impurities are disappeared and all diffraction peaks can be well indexed to the orthorhombic $Pna2_1$ space group of $KTiOPO_4$ (ICDD Card No. 78-1342) for both samples. However, further increment of the PVDF/PTFE amount to 35wt% results in the re-emergence of impurity peaks, thus implying that appropriate amounts of PVDF/PTFE addition are necessary to obtain phase-pure $KVPO_4F$. Considering the cost of material production, the optimum adding amount of PVDF/PTFE is determined to be 15 wt%.

The influences of PVDF and PTFE on morphologies of as-prepared samples are further revealed by SEM images (**Fig. 2i** and **Fig. S5**). Clearly, the sample prepared with 5wt% PVDF addition is composed of closely-packed nanosheets and dense structure, whereas increasing PVDF content results in "house-of-cards" stacking of thinner nanosheets and larger exposed surface area, which is due to the decomposition of PVDF into gaseous substances during calcination and therefore is beneficial to the infiltration of electrolytes. In contrast, large-sized agglomerates with smooth surface were observed for the samples prepared with PTFE, thus further confirms the absence of porous structure (**Fig. S6**).

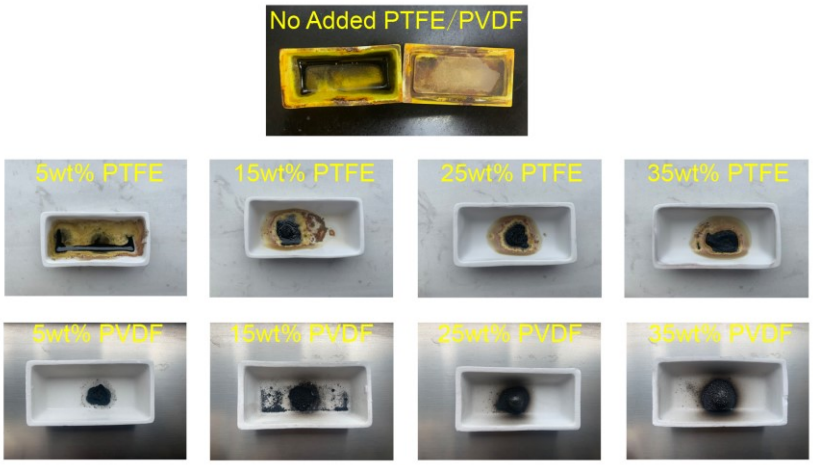

Fig. S3. Photo images of as-prepared samples with addition of different amount PVDF/PTFE.

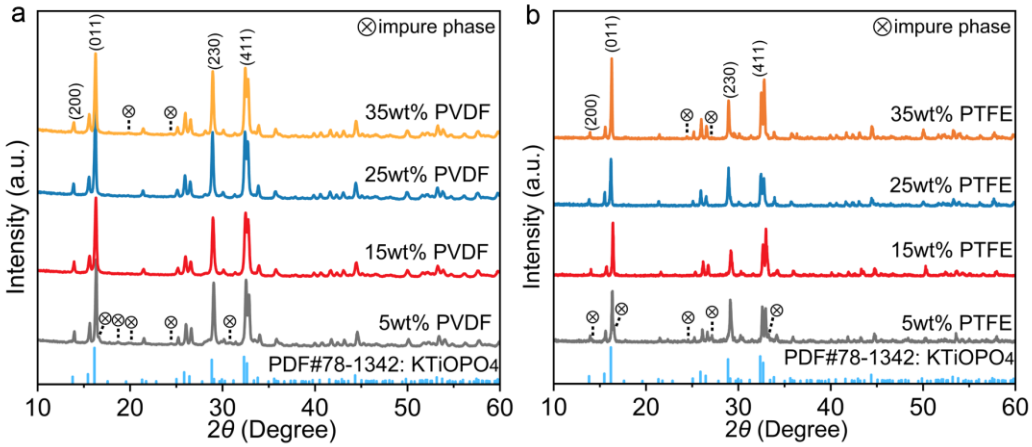

Fig. S4. XRD patterns of $KVPO_4F$ with addition of different amount (a) PVDF and (b) PTFE.

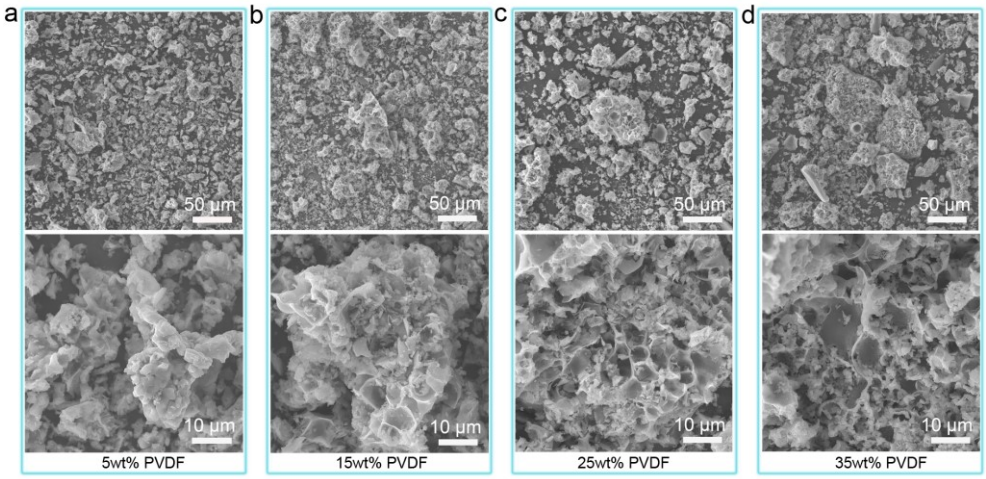

Fig. S5. The SEM images with addition of different amount PVDF.

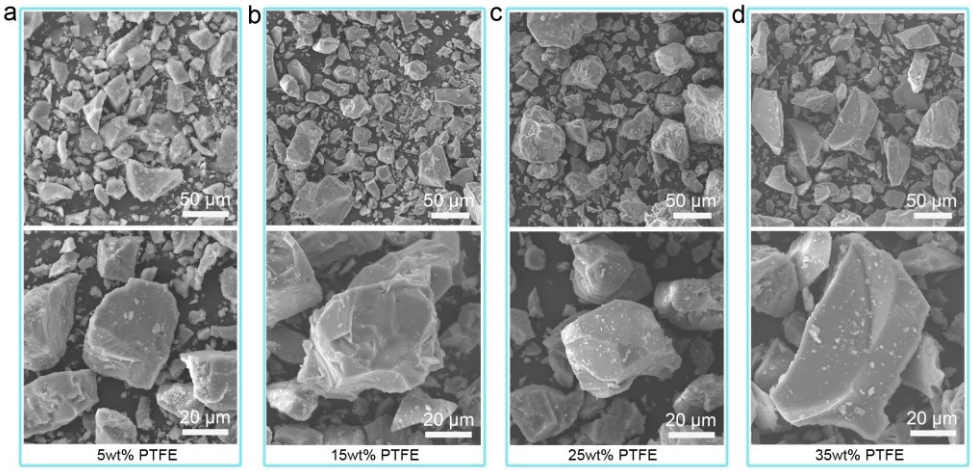

Fig. S6. The SEM images with addition of different amount PTFE.

Supplementary Note 2:

KVPF-CTR was synthesized using a well-known two-step carbothermal reduction (CTR) method based on previous researches,[2-5] and the schematic is shown in **Fig. S7**. In the first step, VPO_4 was obtained by ball milling V_2O_5, $NH_4H_2PO_4$, and acetylene black for 6 hours, followed by heat-treatment at 750 °C for 6 hours under Ar flow in a tube furnace with a ramp of 10 °C min^{-1} (**Fig. S7c**). In the second step, stoichiometric amounts of KF and the as-synthesized VPO_4/C powders were homogeneously mixed and sintered at 750 °C for 3 hours with Ar flow to obtain the black $KVPO_4F$ powders (**Fig. S7d**). Temperature dependent *ex-situ* XRD results show that the $KVPO_4F$ material starts to form when the temperature is raised to 550 °C and the crystallinity becomes stronger at 750 °C. The color, morphology, specific surface area and porous structure of the VPO_4 (**Fig. S7a, b**) and the KVPF-CTR (**Fig. S7g-i**) samples are almost the same.

Moreover, $KVOPO_4$ and $K_2VOP_2O_7$ were also synthesized by using a solid-state reaction method (**Fig. S8**).

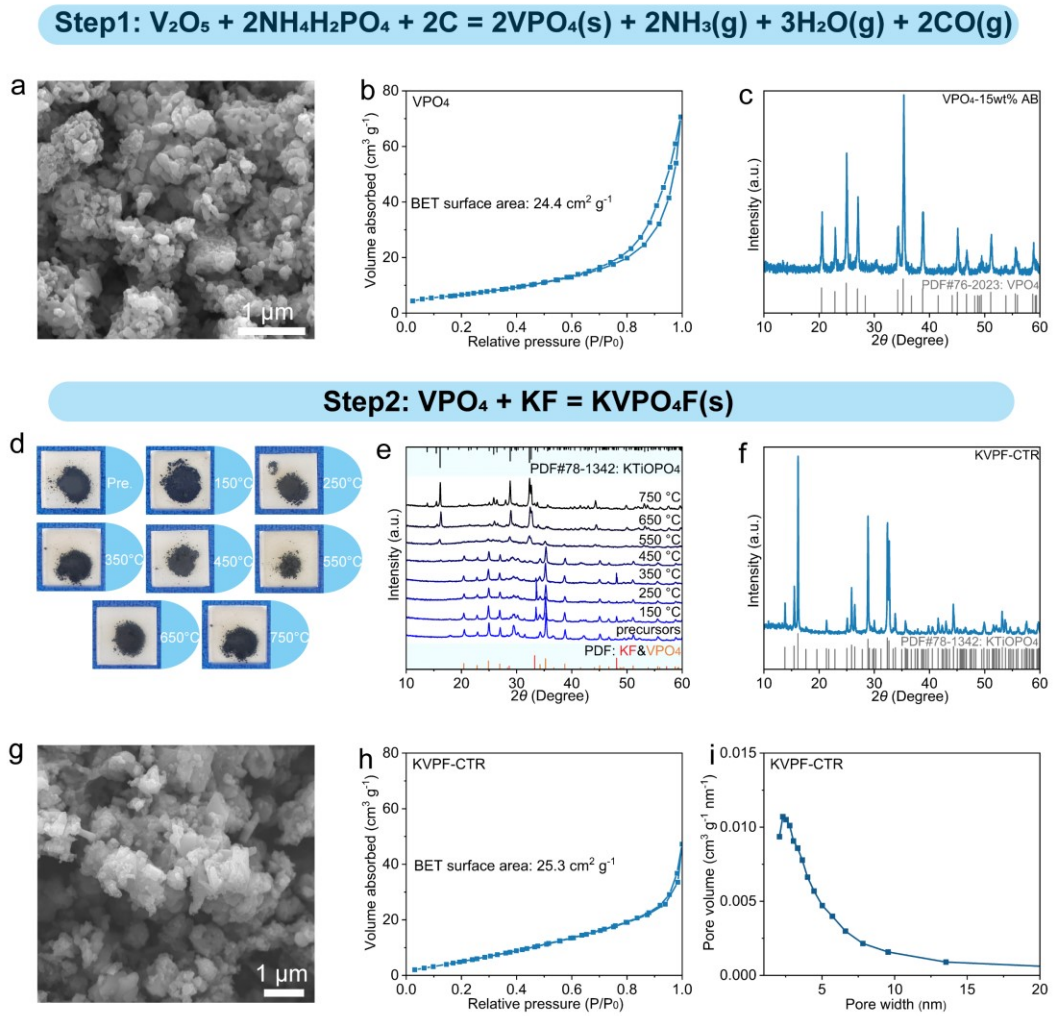

Fig. S7. (a) SEM, (b) N_2 adsorption-desorption isotherm and (c) XRD pattern of VPO_4. (d) Photo images and (e) XRD patterns of as-prepared KVPF-CTR samples with different calcination temperatures. (f) XRD patterns of KVPF-CTR. (g) SEM of KVPF-CTR. (h) N_2 adsorption-desorption isotherm and (i) pore size distributions of KVPF-CTR.

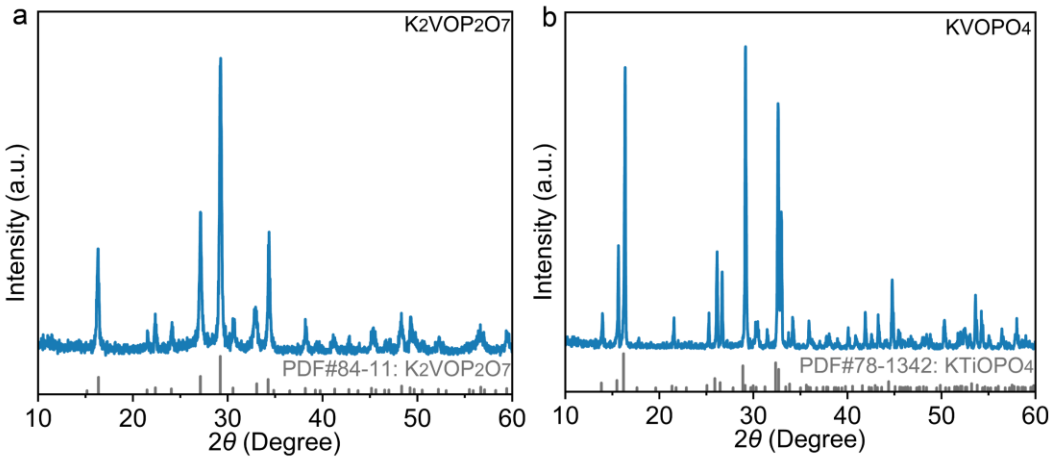

Fig. S8. XRD patterns of (a) $K_2VOP_2O_7$ and (b) $KVOPO_4$.

Supplementary Note 3:

The Rietveld refinements for XRD patterns of both KVPF-PVDF and KVPF-PTFE were performed based on the reported structure model of $KTiOPO_4$ (**Fig. 2a** and **Fig. S9**). The refined parameters are summarized in **Table S1** and **S2**. All bond lengths in KVPF-PVDF are within 2 Å, which is consistent with the usual quasi-symmetric octahedral structure of V^{3+} (inset of **Fig. 2e**). The structure of KVPF-PTFE adopts similar structures built on VO_4X_2 (X is most likely O) octahedra and PO_4 tetrahedra (**Fig. 2g**). In particular, the noncentrosymmetric VO_4X_2 (X is most likely O) octahedra of KVPF-PTFE have highly covalent vanadium-type bonds (V^{4+}=O) that result in both short and long V–O bonds.

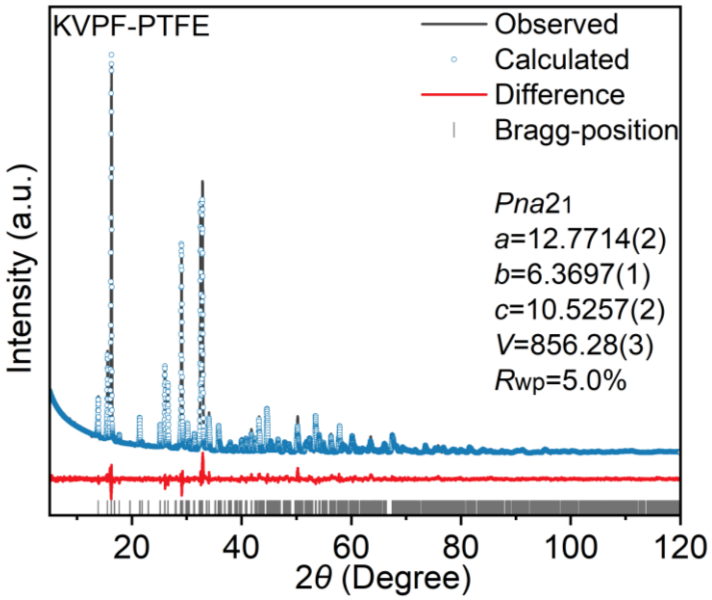

Fig. S9. Rietveld refinement spectrum of KVPF-PTFE.

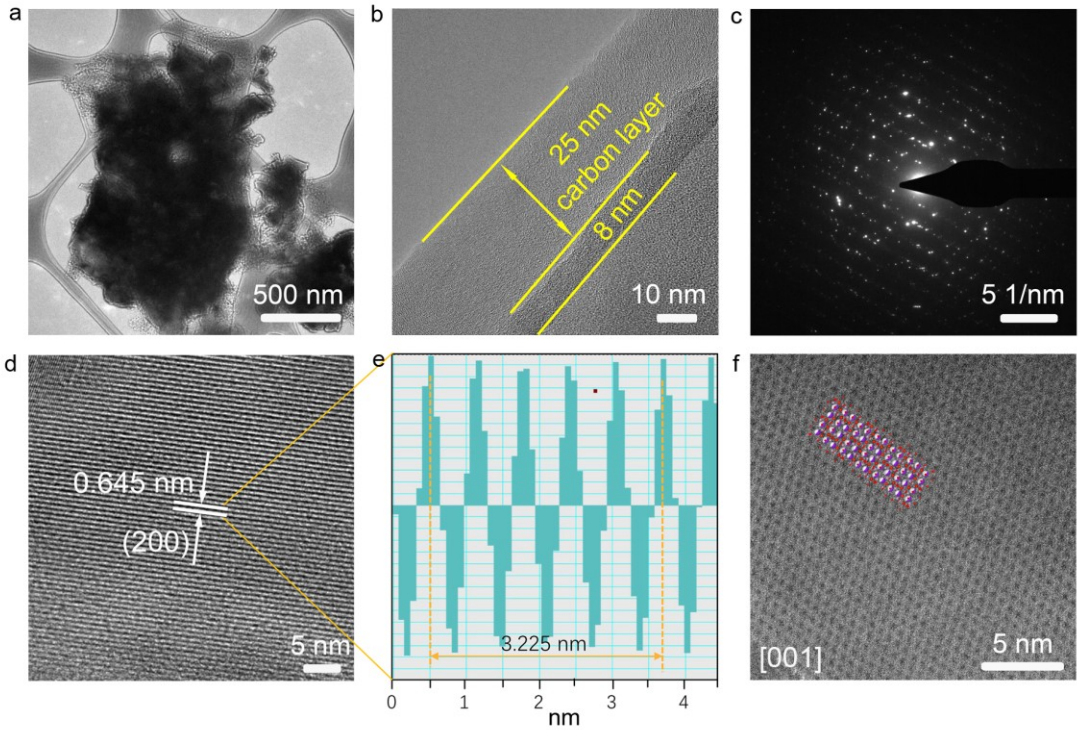

Fig. S10. (a, b) TEM images, (c) SAED pattern, (d, e) HRTEM images, and (f) HAADF-STEM image of KVPF-PVDF.

Supplementary Note 4:

Two characteristic Raman peaks located at 1342 and 1582 cm^{-1} that are corresponding to the D and G bands of carbon materials are observed for KVPF-PVDF (**Fig. 2d**), which can be attributed to the surface-coated carbon that is generated upon thermal decomposition of PVDF. However, the D and G bands are not found in the Raman spectrum of KVPF-PTFE, indicating the absence of surface carbon layer. The carbon–sulfur (CS) analyzer (**Fig. S11a**) also confirms the presence of 3.12wt% carbon in KVPF-PVDF, whereas the carbon content is almost zero (0.01wt%) in KVPF-PTFE. **Fig. S11b** demonstrates how the carbon content changes proportionally with the quantity of PVDF added, highlighting the correlation between these two parameters. Nevertheless, high carbon content could lead to a decrease of the active material content in the electrode, hence decreasing the energy density and specific capacity of the electrode material.

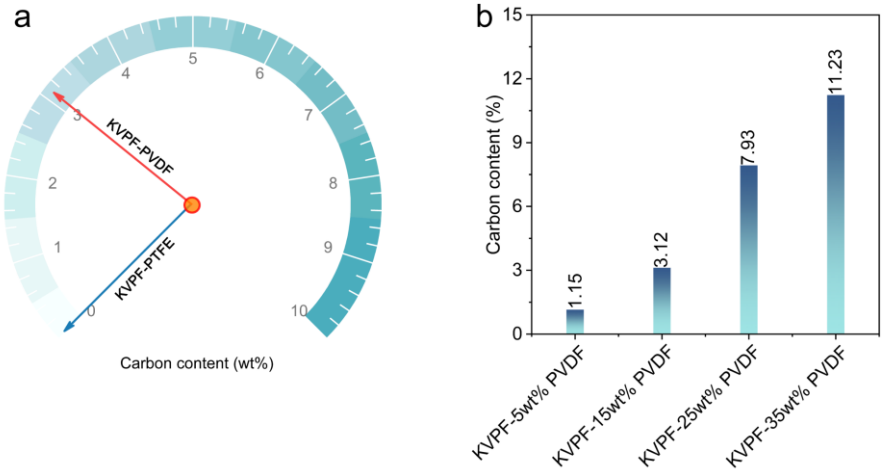

Fig. S11. (a) Plots of carbon content of KVPF-PVDF and KVPF-PTFE. (b) Plots of carbon content of KVPF with addition of different amount PVDF.

Supplementary Note 5:

The nitrogen adsorption-desorption measurements have been performed to characterize pore structures and obtain specific surface areas of as-prepared samples (**Fig. S12**). Clearly, all samples prepared with PVDF addition exhibit typical type IV isotherms, indicating their mesoporous structures according to IUPAC classification. The obviously increased specific surface area and mesopore volume with increasing PVDF content has been observed, which is mainly due to the larger decomposition amount of PVDF upon sintering and is consistent with their SEM images, i.e., larger volume change after calcination (as shown in **Fig. S3**, the samples prepared with increased PVDF content exhibit same mass but obviously larger volume) and obviously smaller tap/bulk density (**Fig. S13**).

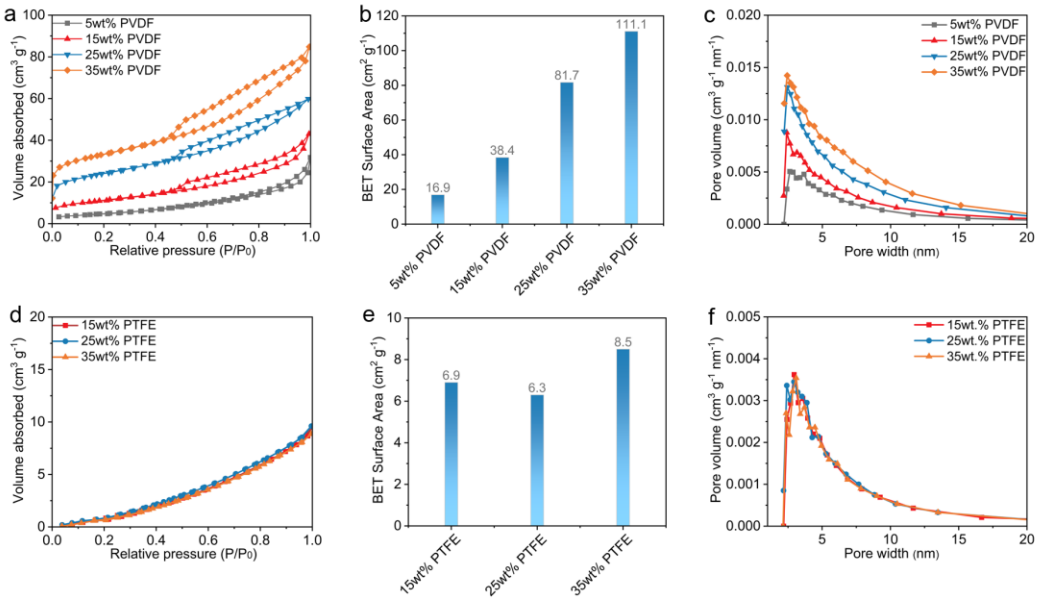

Fig. S12. (a, d) N_2 adsorption–desorption isotherms, (b, e) BET specific surface area, and (c, f) pore size distributions with different amounts of PVDF/PTFE added.

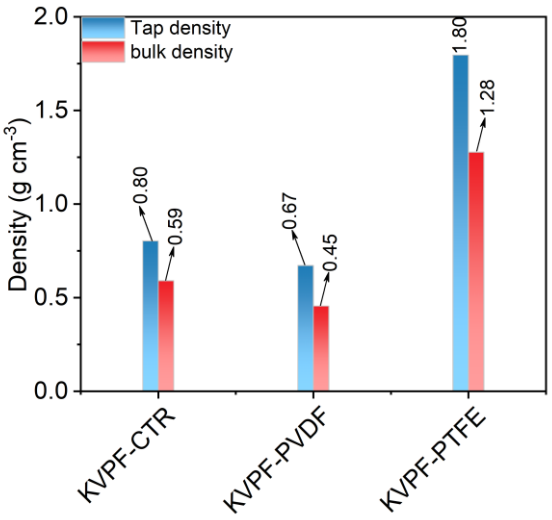

Fig. S13. The tap density and bulk density of KVPF-PVDF, KVPF-PTFE and KVPF-CTR.

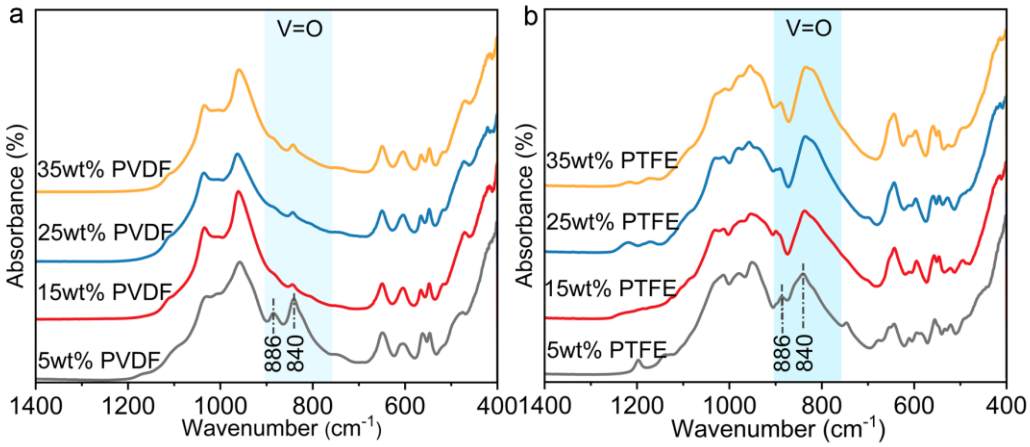

Fig. S14. FTIR patterns of KVPF with addition of different amount (a) PVDF and (b) PTFE.

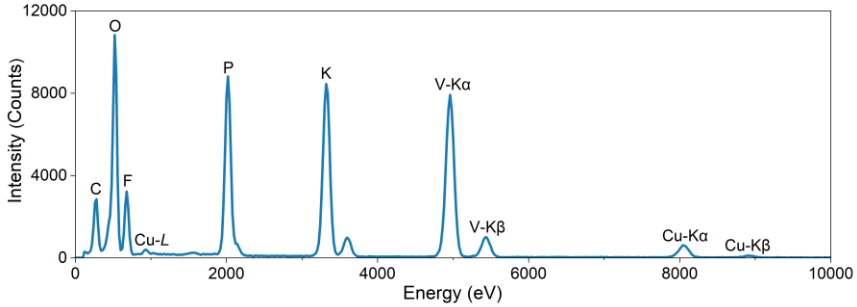

Fig. S15. STEM-EDS spectrum of KVPF-PVDF.

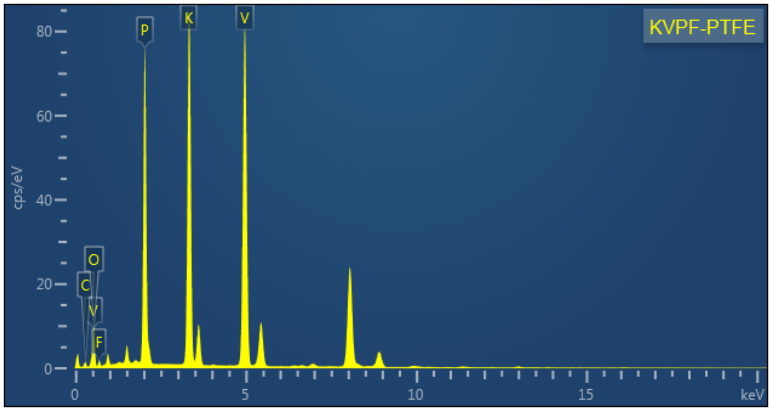

Fig. S16. STEM-EDS spectrum of KVPF-PTFE.

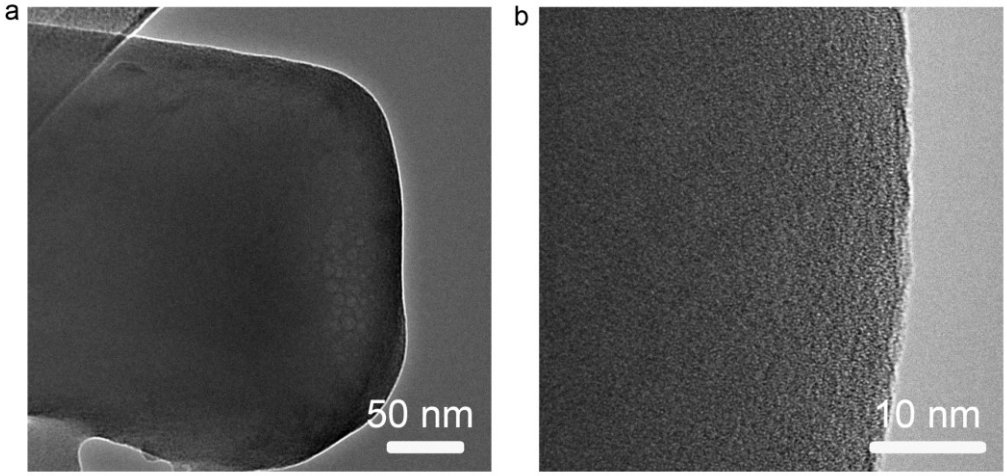

Fig. S17. (a, b) TEM images of KVPF-PTFE.

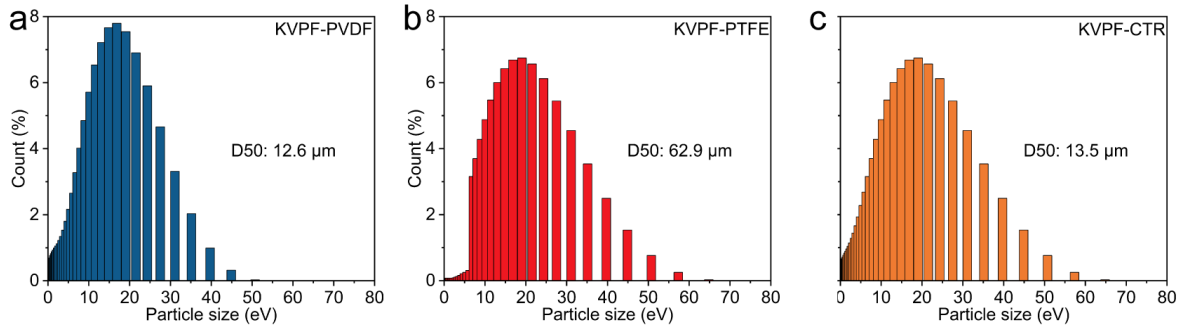

Fig. S18. Particle size distribution curves of (a) KVPF-PVDF, (b) KVPF-PTFE, and (c) KVPF-CTR.

Fig. S19. Digital images of the synthesized 200 g scale KVPF-PVDF products.

Supplementary Note 6:

The crystal growth, morphologies, and phases of the synthesized materials were evaluated through TG-MS, XRD, and SEM analyses. TG-DSC curve for KVPF-PVDF/KVPF-PTFE precursors exhibits three distinct regions (**Fig. S20**). The initial endothermal peak (Peak A, ~189 °C) is linked to $NH_4H_2PO_4$ decomposition, resulting in $H_4P_2O_7$, NH_3 and H_2O generation, which leading to a weight loss of ~12.1% for KVPF-PVDF and ~11.6% for KVPF-PTFE due to the release of gaseous substances **(Eq. S1**/**Eq. S5**, Page 16). In this stage (Stage I), KVPF-PVDF/KVPF-PTFE precursors transform from compact particles to lose porous structures (**Fig. S22** and **Fig. S24**). Further increasing the calcination temperature results in two additional weight losses, indicating the decomposition of PVDF/PTFE and forming the final KVPF-PVDF/KVPF-PTFE products. During this stage (Stage II), the XRD and SEM of two KVPF-PVDF/KVPF-PTFE precursors exhibit distinct responses to temperature, suggesting two different reaction pathways. For KVPF-PVDF precursors, the material becomes more porous with rising temperature, eventually forming a honeycomb structure at 750 °C (**Fig. S22**). In contrast, KVPF-PTFE precursors gradually changed from a loose and porous structure to a dense structure, and finally to large-sized particles with a smooth surface (**Fig. S24**). Notably, upon increasing the temperature to 850 °C, impurity peaks of $K_3Fe_3(PO_4)_4{\cdot}H_2O$-type $K_3V_3(PO_4)_4$ begin to emerge due to fluorine volatilization. At 950 °C, the $KVPO_4F$ is completely decomposed into $K_3Fe_3(PO_4)_4{\cdot}H_2O$-type $K_3V_3(PO_4)_4$, highlighting the thermal stability of the material and the importance of controlling the calcination temperature to control the phase. This phenomenon is also reflected by changes of the material morphology (from a honeycomb structure to a dense structure, **Fig. S22**).

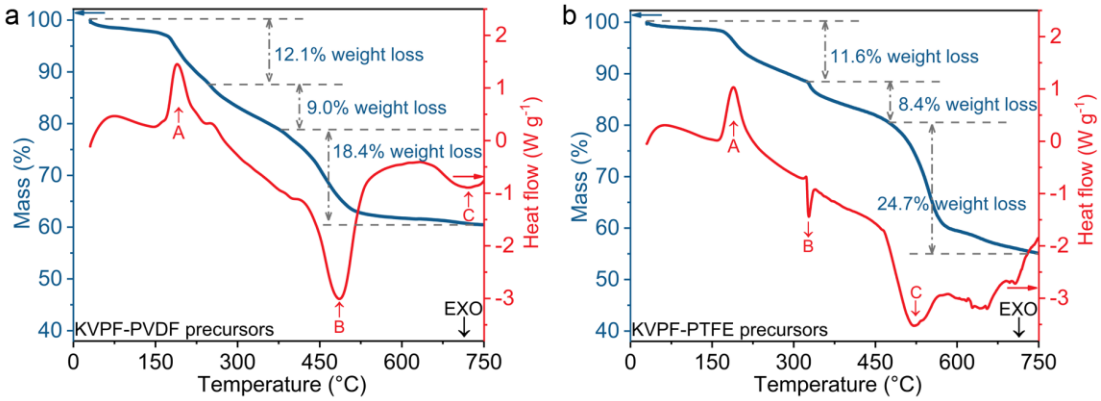

Fig. S20. TG/DSC curves of the (a) KVPF-PVDF and (b) KVPF-PTFE precursors.

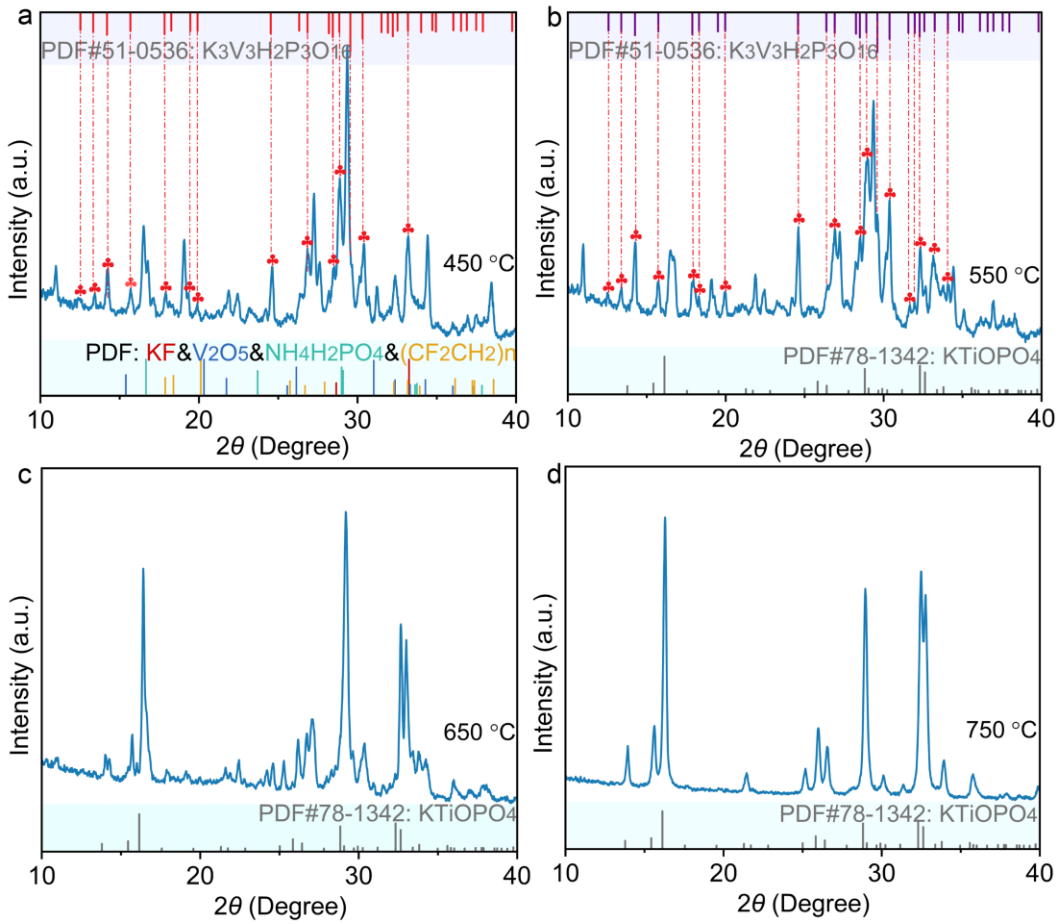

Fig. S21. XRD pattern of KVPF-PVDF precursors with different calcination temperatures of (a) 450 °C, (b) 550 °C, (c) 650 °C and (d) 750 °C.

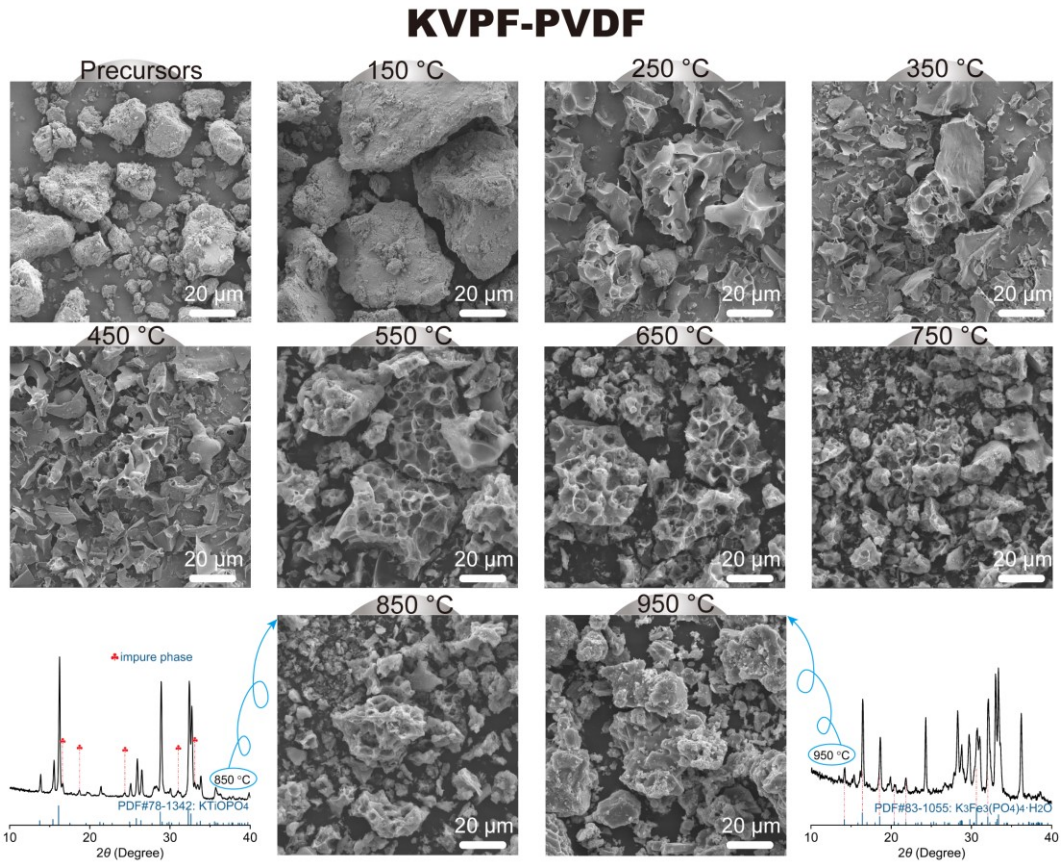

Fig. S22. SEM patterns at different calcination temperatures of KVPF-PVDF.

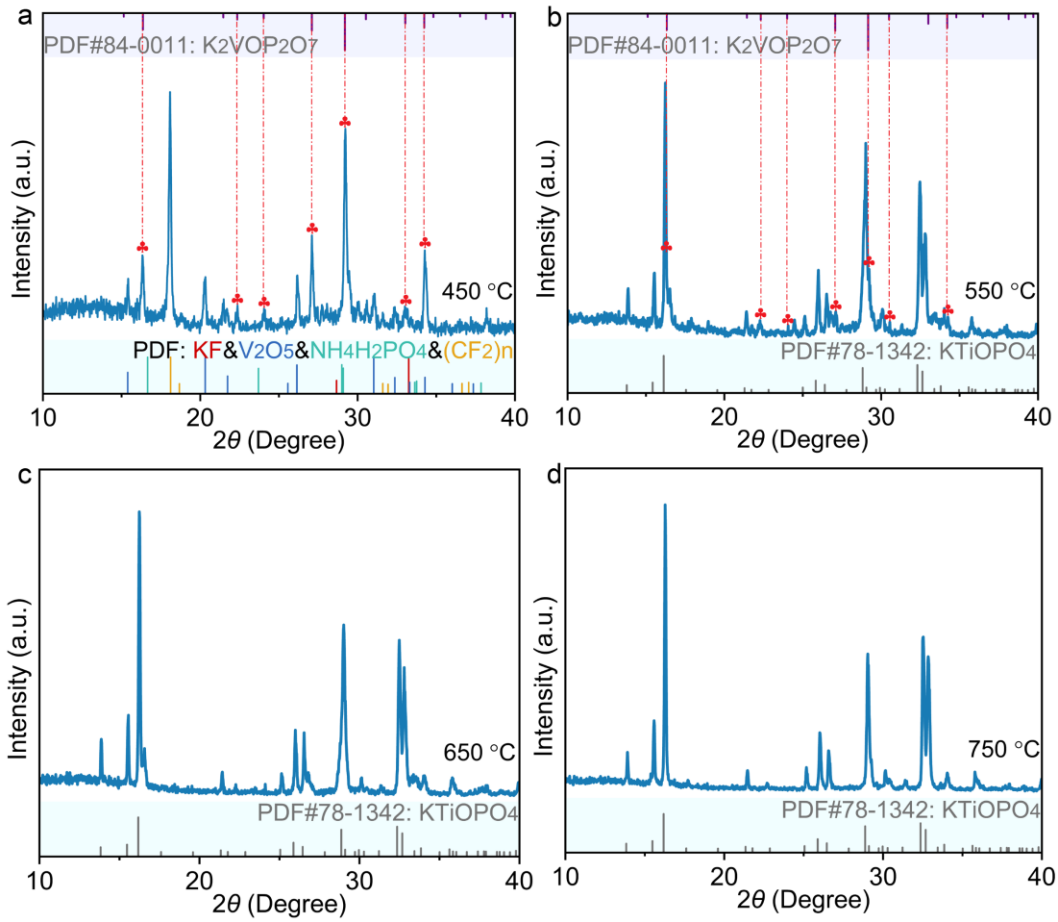

Fig. S23. XRD pattern of KVPF-PTFE precursors with different calcination temperatures of (a) 450 °C, (b) 550 °C, (c) 650 °C and (d) 750 °C.

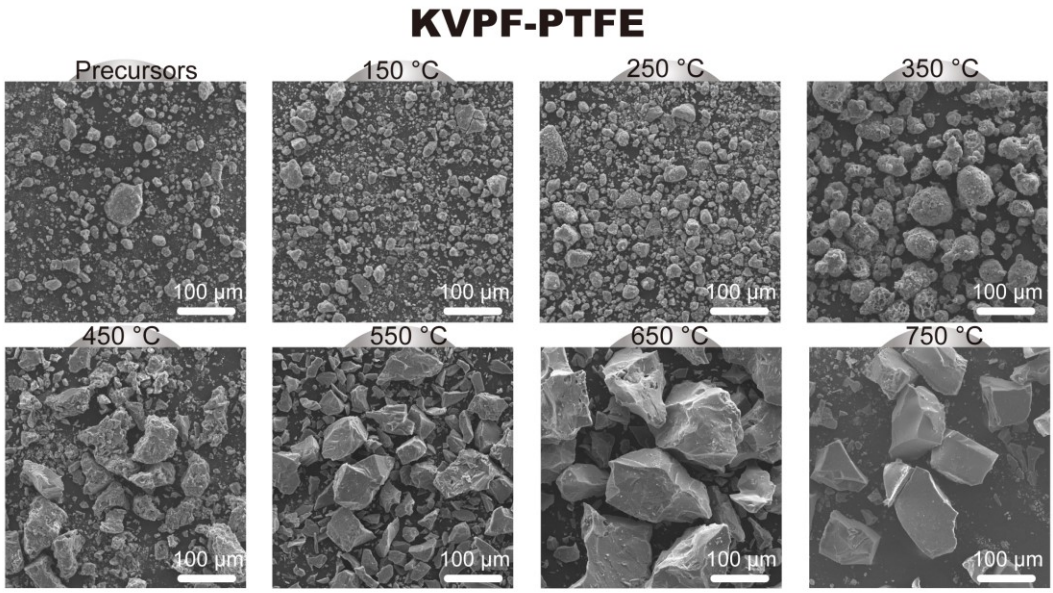

Fig. S24. SEM patterns at different calcination temperatures of KVPF-PTFE.

A schematic mechanism of structural and compositional evolution in the synthesis process can be described as follows:

For KVPF-PVDF:

Eq. S1: $2NH_4H_2PO_4 = 2NH_3+H_4P_2O_7+H_2O$

Eq. S2: $12KF+12NH_3+6H_4P_2O_7+6V_2O_5 = 4K_3V_3H_2P_3O_{16}+12HF+4O_2+6N_2+20H_2$

Eq. S3: $(CH_2CF_2)_n \rightarrow :CH_2 + :CF_2$

$n{:}CH_2 \rightarrow \cdot CH_2CH_2CH_2CH_2 \cdot$

$2{:}CF_2 \rightarrow C_2F_4$

Eq. S4: $3C_2F_4+4\cdot CH_2CH_2CH_2CH_2\cdot+4K_3V_3H_2P_3O_{16} = 12KVPO_4F+18C+16H_2O$

For KVPF-PTFE:

Eq. S5: $12NH_4H_2PO_4 = 12NH_3+6H_4P_2O_7+6H_2O$

Eq. S6: $6H_4P_2O_7+2NH_3+12KF+3V_2O_5 = 6K_2VOP_2O_7+N_2+12HF+9H_2O$

Eq. S7: $(CF_2CF_2)_n \rightarrow 2{:}CF_2$

$2{:}CF_2 \rightarrow C_2F_4$

Eq. S8: $2K_2VOP_2O_7+2HF = 2KVOPO_4+2KF+P_2O_5+H_2O$

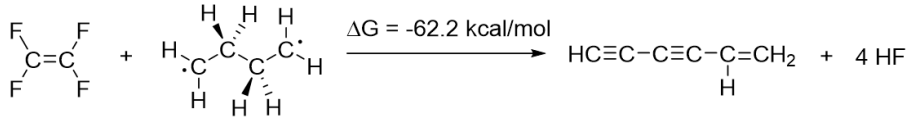

Fig. S25. Computed free energy profiles (in kcal/mol) at the B3LYP+D3(BJ)/6-311+G(2d,p)//B3LYP+D3(BJ)/6-31G** level of theory.

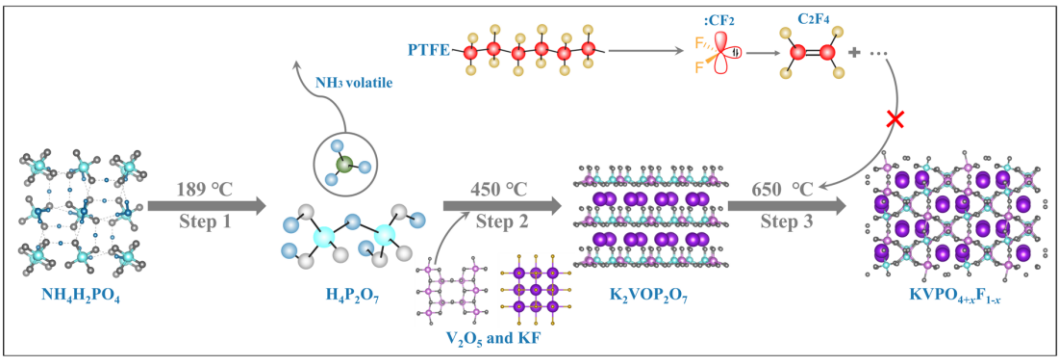

Fig. S26. Mechanism for the synthesis of KVPF-PTFE.

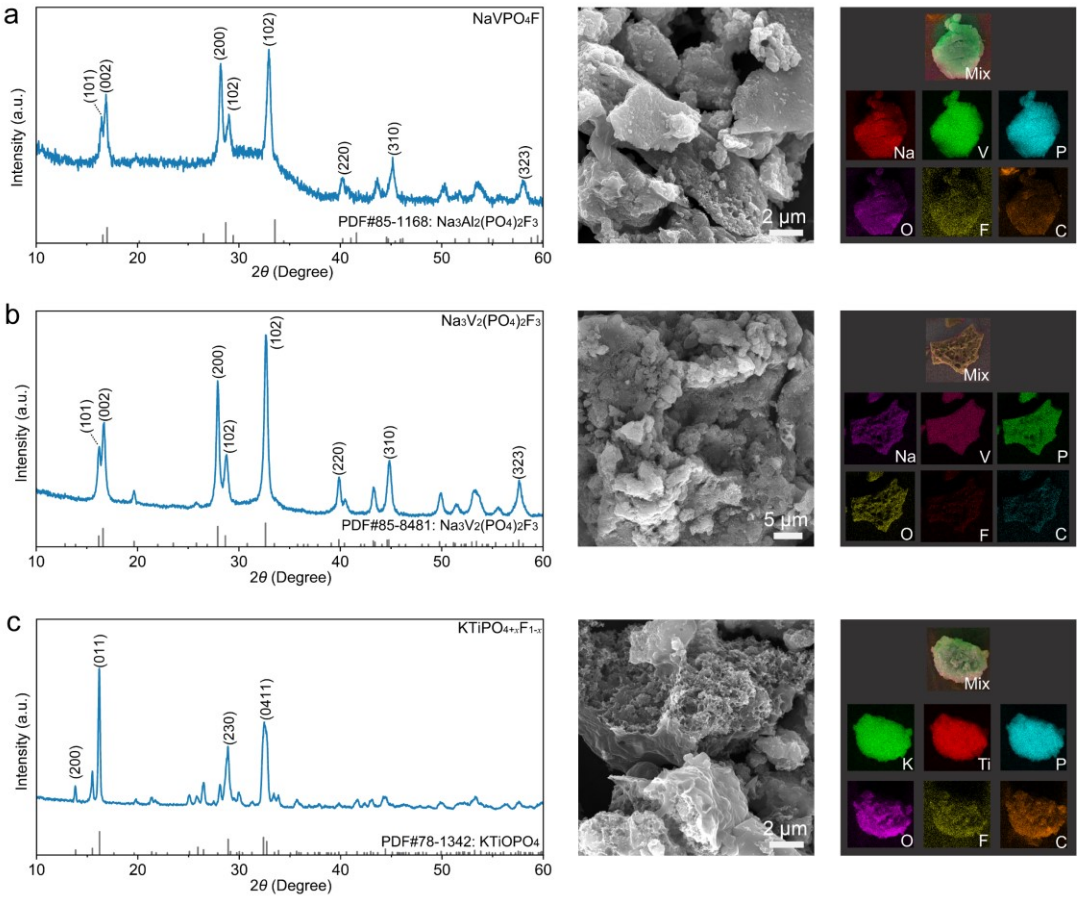

Fig. S27. The preparation of other phase-pure $A_xM_y[(XO_m)_n]_zF_a$. Characterizations of (a) $NaVPO_4F$, (b) $Na_3V_2(PO_4)_2F_3$ and (c) $KTiPO_{4+x}F_{1-x}$.

Supplementary Note 7:

It should be note that Ti^{4+} cannot be completely reduced to Ti^{3+} by carbon at only 750°C (which may have mixed Ti^{3+} and Ti^{4+} in $KTiPO_{4+x}F_{1-x}$). To support this point, we have conducted supplementary experiments using ion-selective electrode (ISE) method to determine the F content and STEM-EELS to confirm the valence of Ti. Based on the ISE test, the fluorine content of the $KTiPO_{4+x}F_{1-x}$ sample was found to be 22%, so the empirical formula for $KTiPO_{4+x}F_{1-x}$ should be $KTiPO_{4.78}F_{0.22}$. To verify the valence state of Ti in $KTiPO_{4.78}F_{0.22}$, we obtained STEM-EELS profiles of TiO_2, Ti_2O_3, and $KTiPO_{4.78}F_{0.22}$ (**Fig. S28**). In general, the formation of the orbital order results from the band split near the Fermi level. As for TiO_2, crystal field splits Ti *3d* bands to e_g and t_{2g} bands, but not in Ti_2O_3. Usually, we can determine the valency of Ti by the splitting of Ti $L_{2,3}$ edges. Based on the EELS results, $KTiPO_{4.78}F_{0.22}$ exhibits mixed Ti^{3+} and Ti^{4+}, thus confirms the partial reduction of Ti.

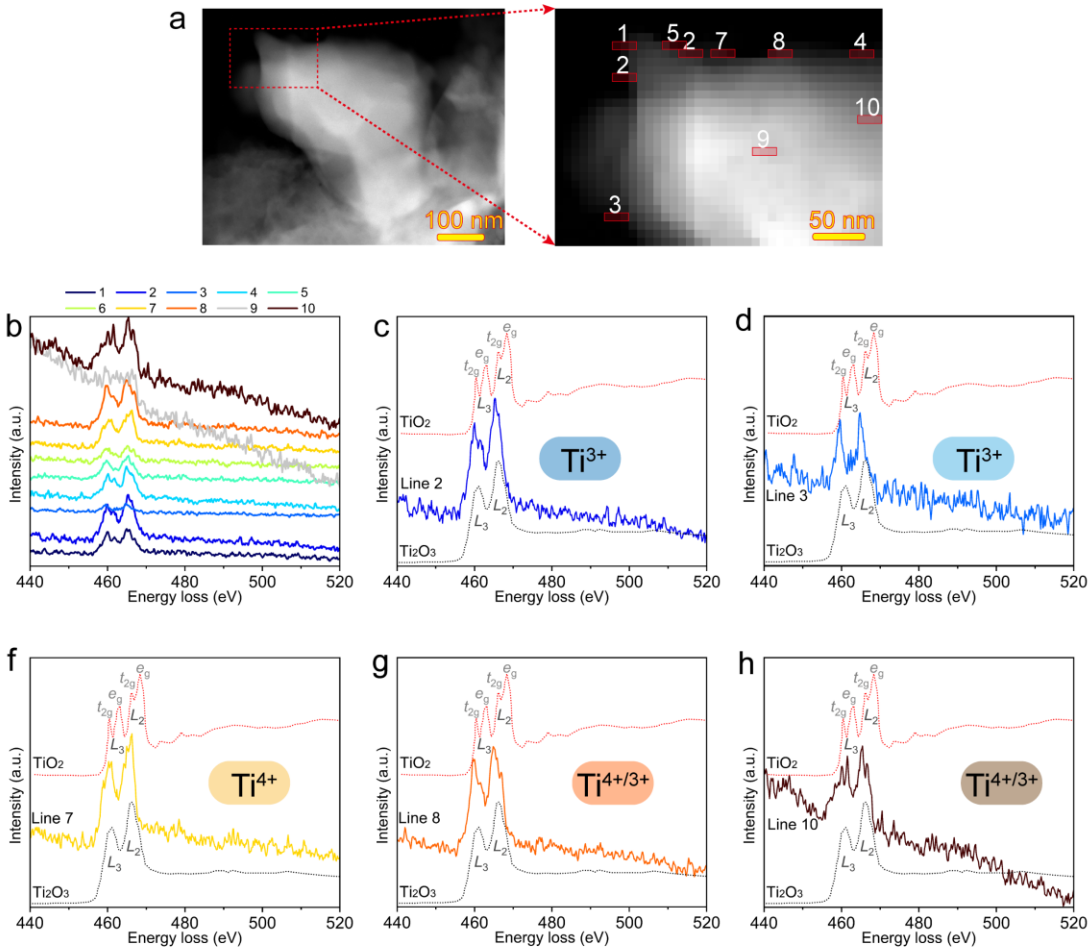

Fig. S28. (a, b) For statistical significance, analysis is performed at a particle size of 60 × 30 nm. (b-h) The STEM-EELS profiles for Ti $L_{2,3}$ of $KVPO_{4.78}F_{0.22}$.

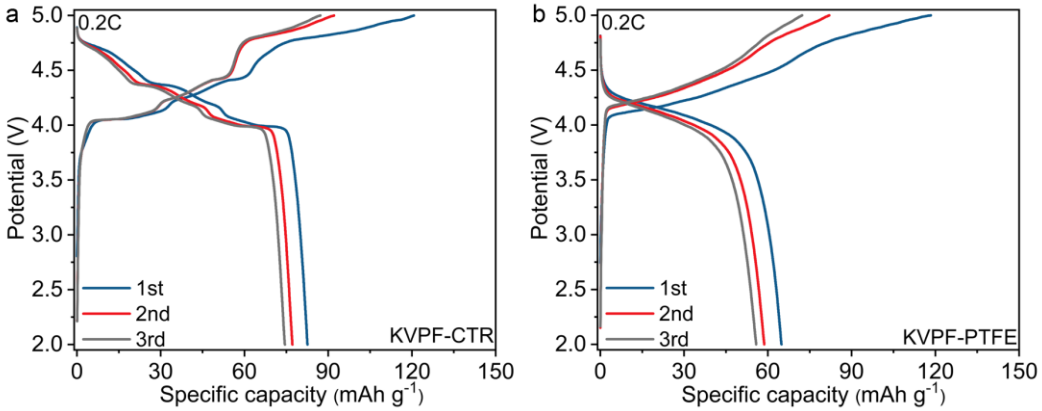

Fig. S29. Galvanostatic charging/discharging profiles of (a) KVPF-CTR and (b) KVPF-PTFE at 0.2C.

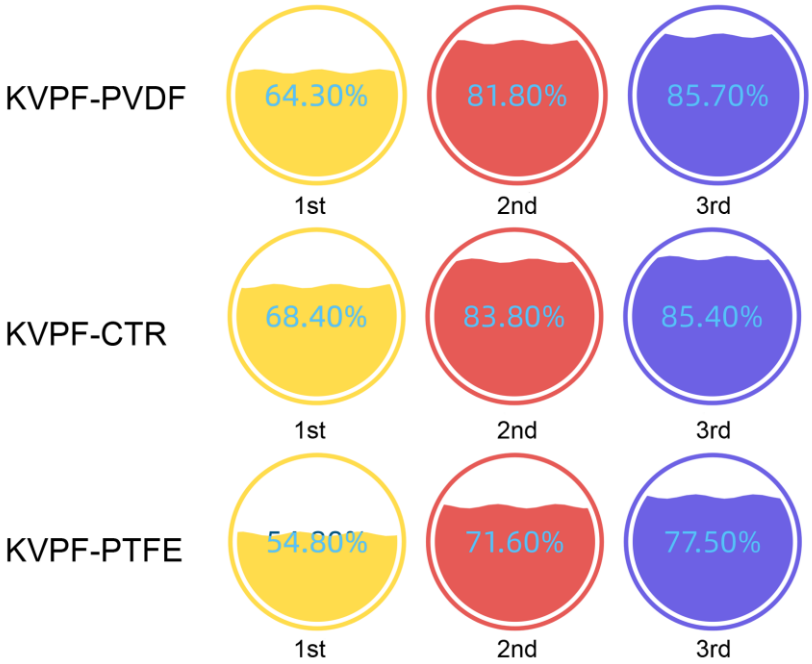

Fig. S30. Comparison of the coulombic efficiency of KVPF-PVDF, KVPF-CTR and KVPF-PTFE at 0.2C for initial three cycles.

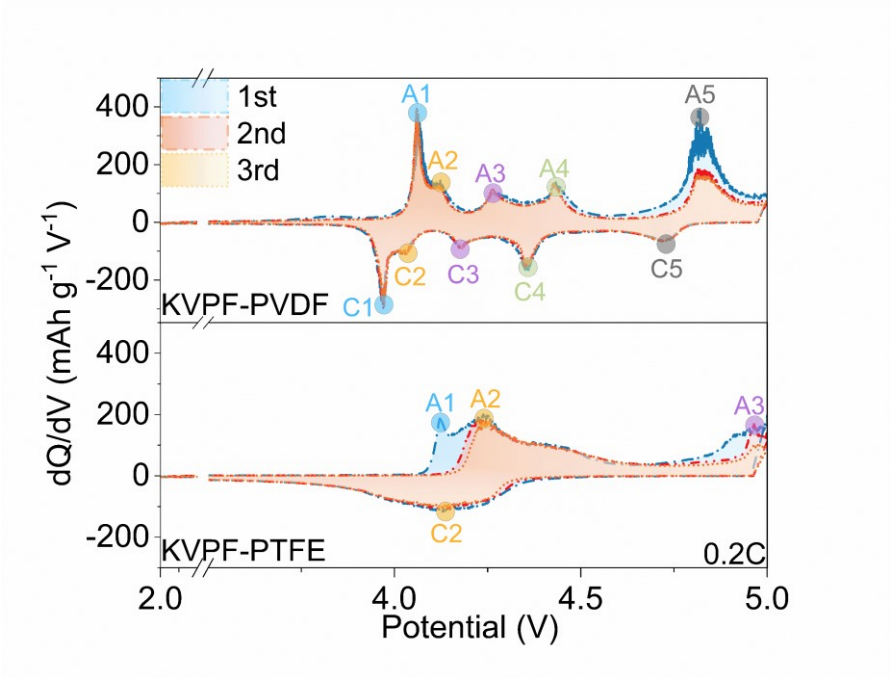

Fig. S31. dQ/dV plots of KVPF-PVDF and KVPF-PTFE at 0.2C.

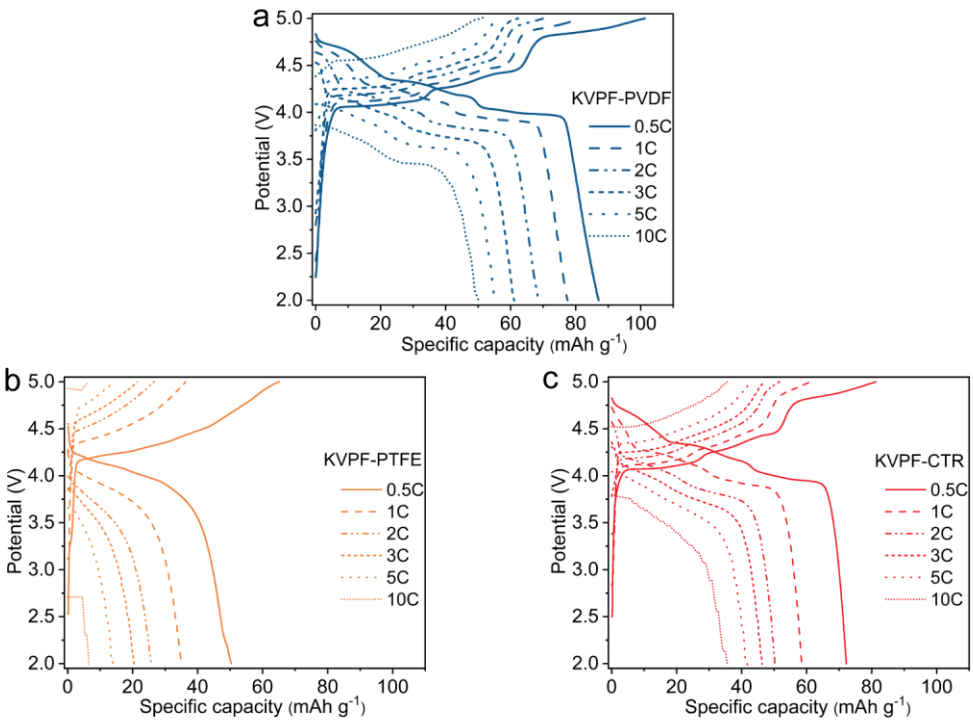

Fig. S32. Discharging/charging curves of (a) KVPF-PVDF, (b) KVPF-PTFE and (c) KVPF-CTR at different current densities.

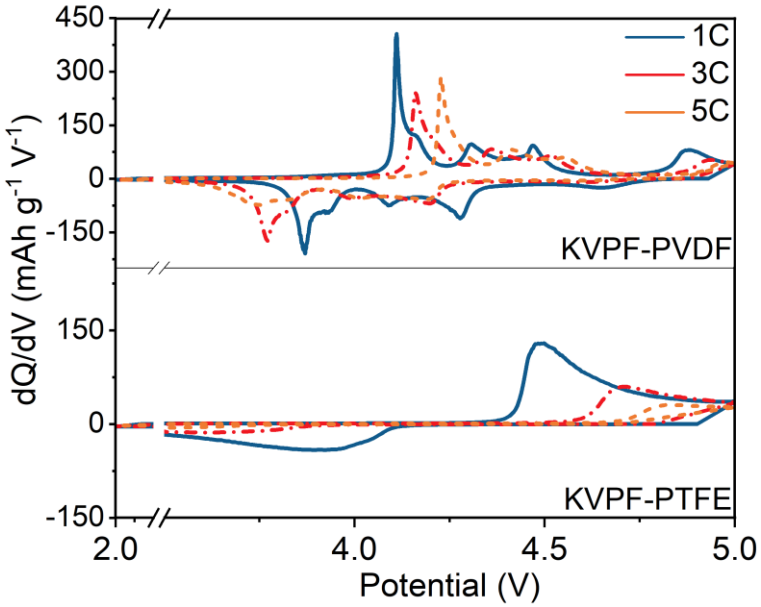

Fig. S33. dQ/dV plots of KVPF-PVDF and KVPF-PTFE under different current densities.

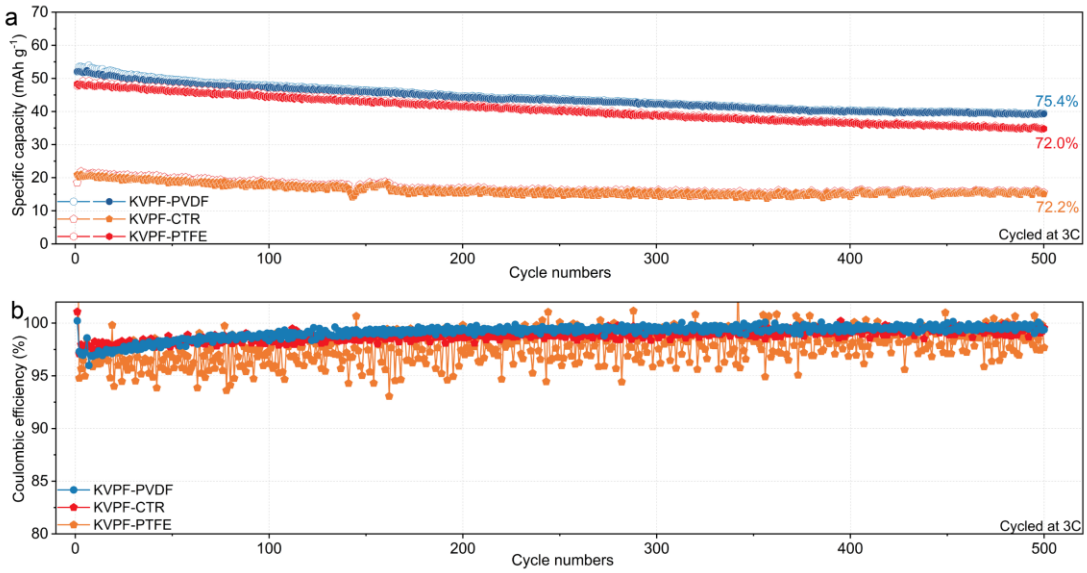

Fig. S34. (a) Cyclability and (b) Coulombic efficiency of KVPF-PVDF, KVPF-CTR and KVPF-PTFE at 3C.

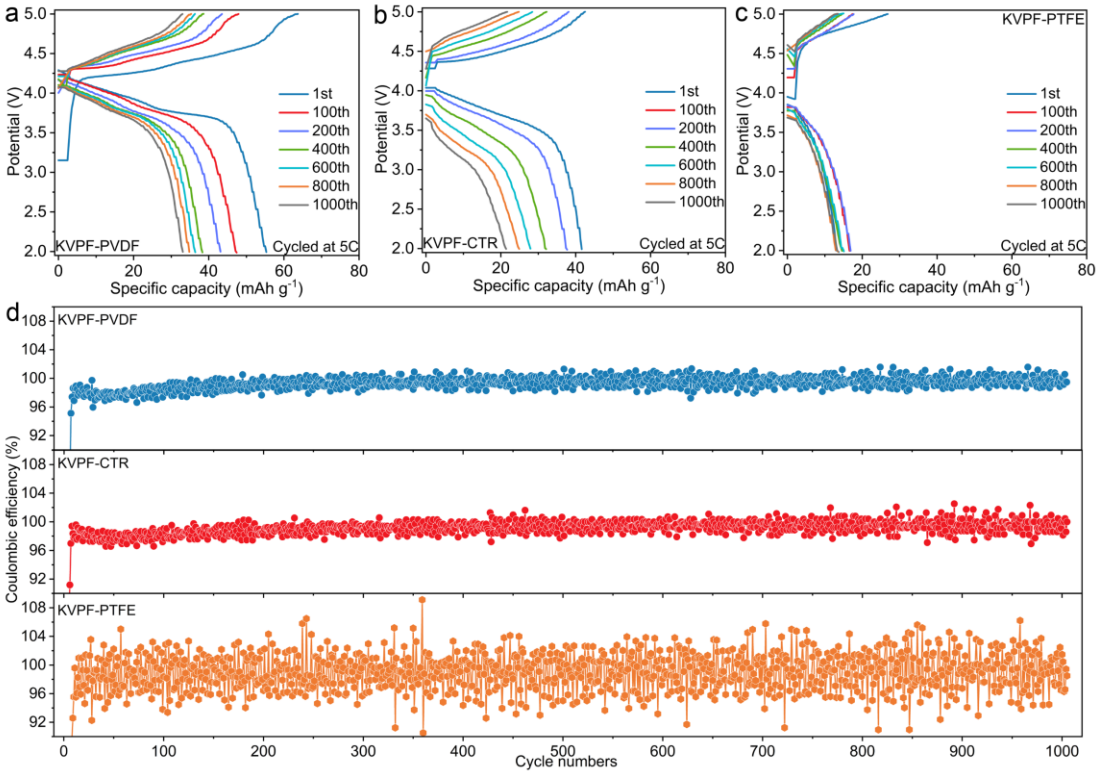

Fig. S35. (a, b, c) Cyclability curves and (d) Coulombic efficiency of KVPF-PVDF, KVPF-CTR and KVPF-PTFE at 5C.

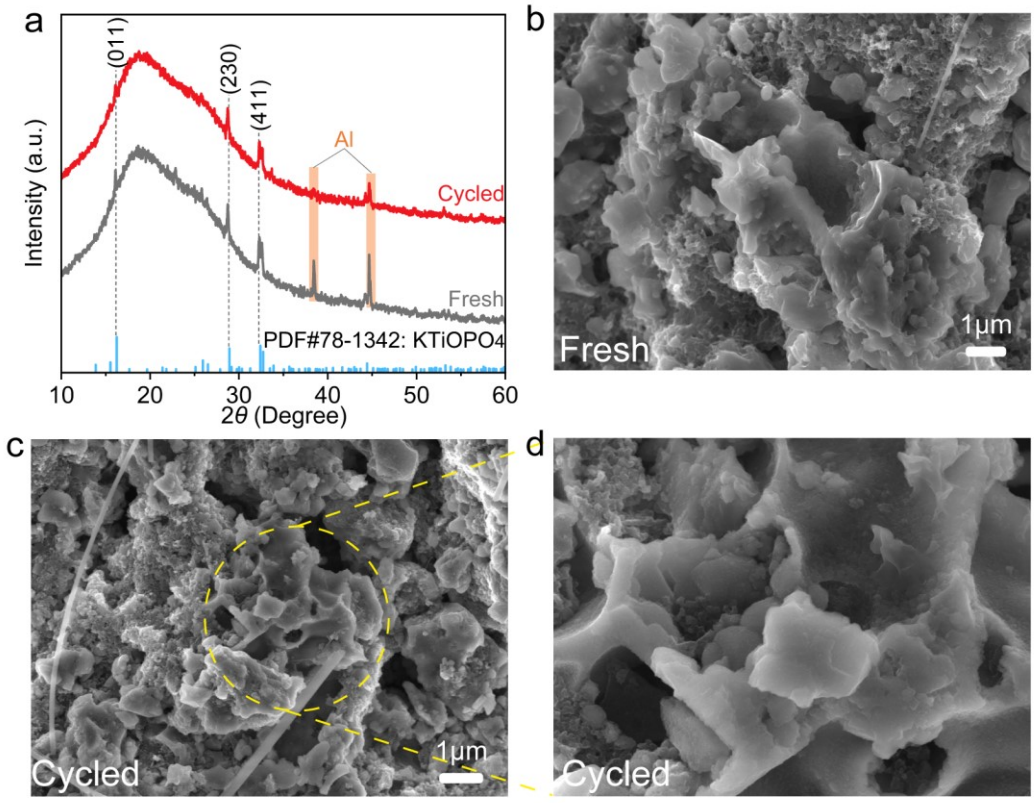

Fig. S36. (a) *Ex-situ* XRD and (b, c, d) *Ex-situ* SEM patterns of KVPF-PVDF.

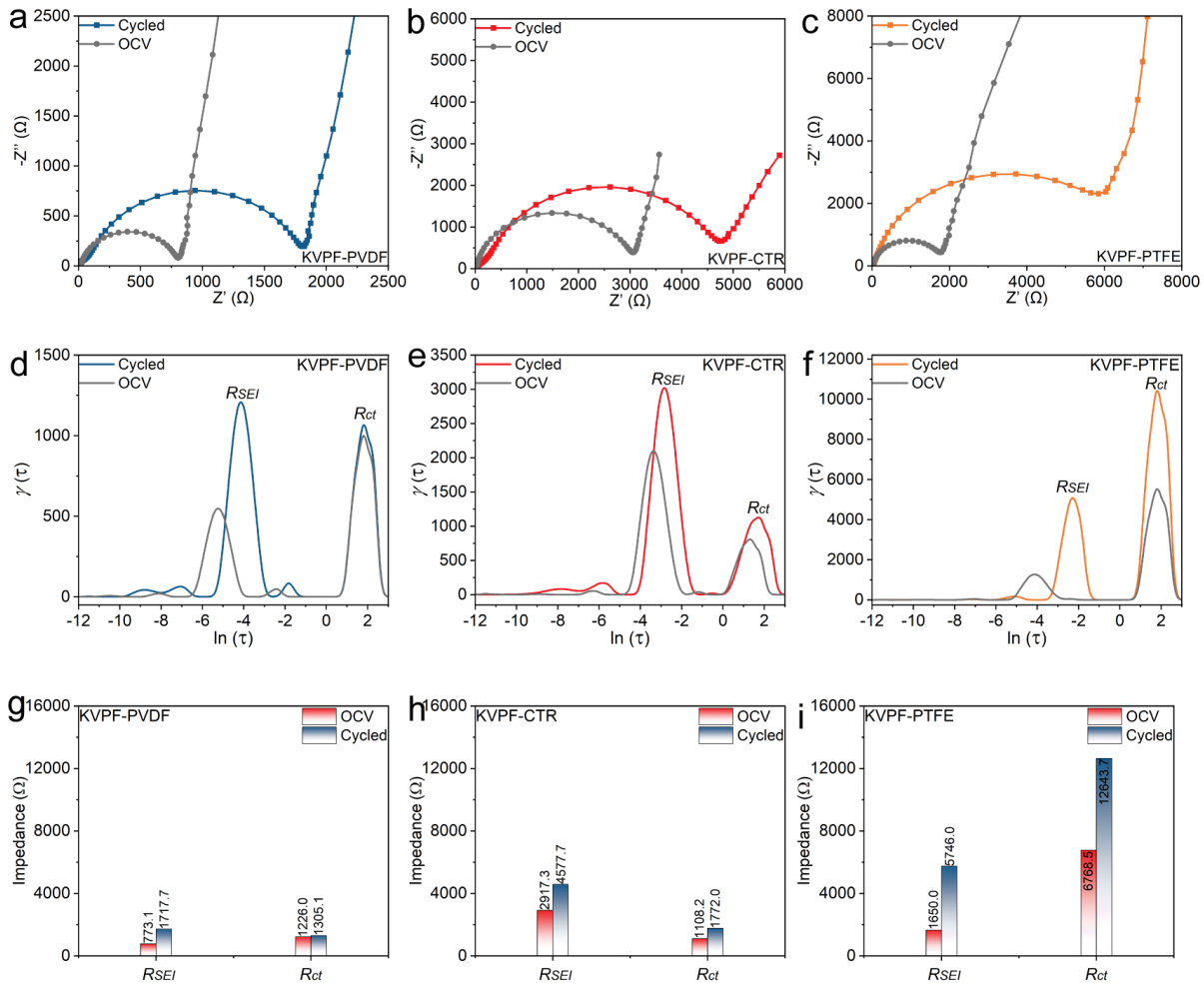

Fig. S37. *Ex-situ* EIS Nyquist plots and corresponding DRTs of (a, d, g) KVPF-PVDF, (b, e, h) KVPF-CTR and (c, f, i) KVPF-PTFE. As shown in **Fig. S37**, both R_{ct} and R_{SEI} of KVPF-PVDF remained relatively stable throughout the cycling process, which are obviously lower than both KVPF-CTR and KVPF-PTFE, indicating that the KVPF-PVDF cell maintained excellent kinetics even after 1000 cycles.

Supplementary Note 8:

In case of electrochemical performance, as we all know, the electrochemical performance of electrode materials is influenced by a multitude of factors, including charge-discharge window, carbon content, phase purity, particle size, electrode architecture, porosity and electrolyte, etc.

Charge-discharge window: Currently, one of the challenges with $KVPO_4F$ is that it undergoes severe oxidative decomposition when paired with conventional carbonate-based electrolytes at high voltages (>4.5V).[2,4-6] Although narrowing the charge-discharge window could alleviate electrolyte decomposition, it can also result in a significant decrease in reversible capacity at low current density due to inadequate redox reactions of $V^{3+}_{trans} \leftrightarrow V^{4+}_{trans}$ in C5/A5, as demonstrated in **Fig. S38a-c**, which is also consistent with the previous findings.[2,4] However, at higher current densities of 5C, the capacity and capacity retention difference between the two charge-discharge windows becomes less noticeable (**Fig. S38d-f**). This is because the large polarization effect leads to unrealized redox reactions (C5/A5) in the high voltage section (>4.8V).

Porosity and carbon content: Despite the fact that the specific surface area of the material with 25% PVDF content is about 2.1 times higher than that of the sample with 15% PVDF content (**Fig. S11b**), more carbon was also generated in KVPF-25% PVDF (7.93% carbon content for KVPF-25% PVDF as tested by carbon–sulfur analyzer, **Fig. S11b**) compared to the KVPF-15% PVDF sample. In this case, high carbon content leads to a decrease of the active material content in the electrode, hence decreasing the energy density and specific capacity of the electrode material (**Fig. S39**).

Phase purity: The morphology and purity of $KVPO_4F$ are significantly impacted by the calcination temperature, which in turn plays a critical role in determining the electrochemical performance. Hence, controlling the calcination temperature is essential for tailoring the morphology and purity of the material (**Fig. S21** and **S22**), and optimizing its electrochemical performance. The relationship between calcination temperature and electrochemical performance of KVPF-PVDF was showed in **Fig. S40**.

Mass loading: It should be noted that increasing the mass loading can have a detrimental effect on the charge transport kinetics, thereby affecting the rate capacity. The relationship between mass loadings of the active materials and electrochemical performance of KVPF-PVDF, KVPF-PTFE, and KVPF-CTR was showed in **Fig. S41-S43**.

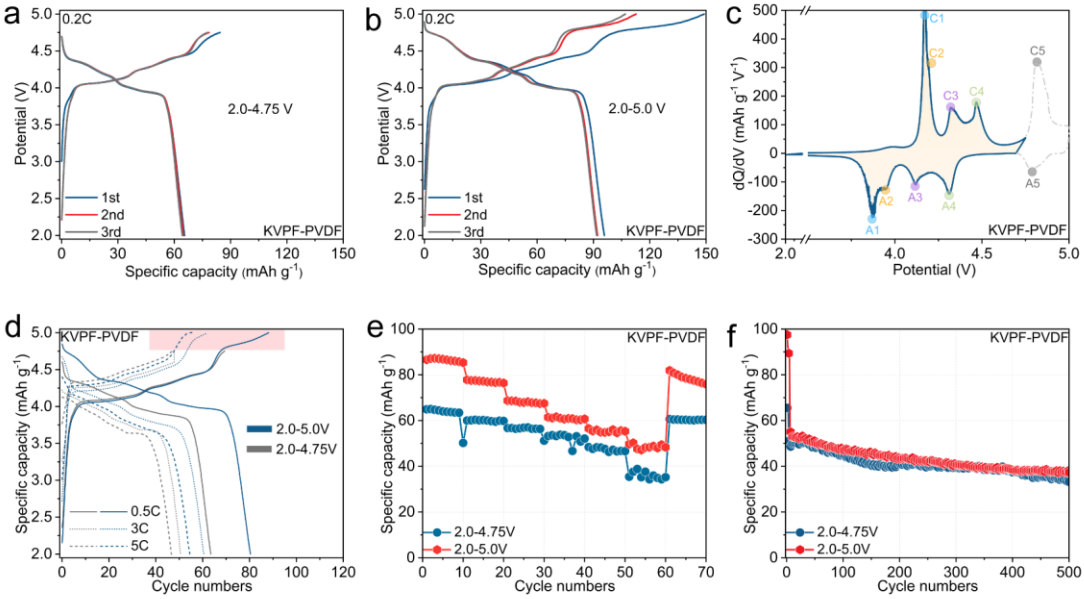

Fig. S38. Galvanostatic charging/discharging profiles of KVPF-PVDF under different charge-discharge window of (a) 2-4.75 V and (b) 2-5.0 V. (c) dQ/dV plots of KVPF-PVDF under different charge-discharge window. (d, e) Rate capability. (g) Long-term cyclability at 5C.

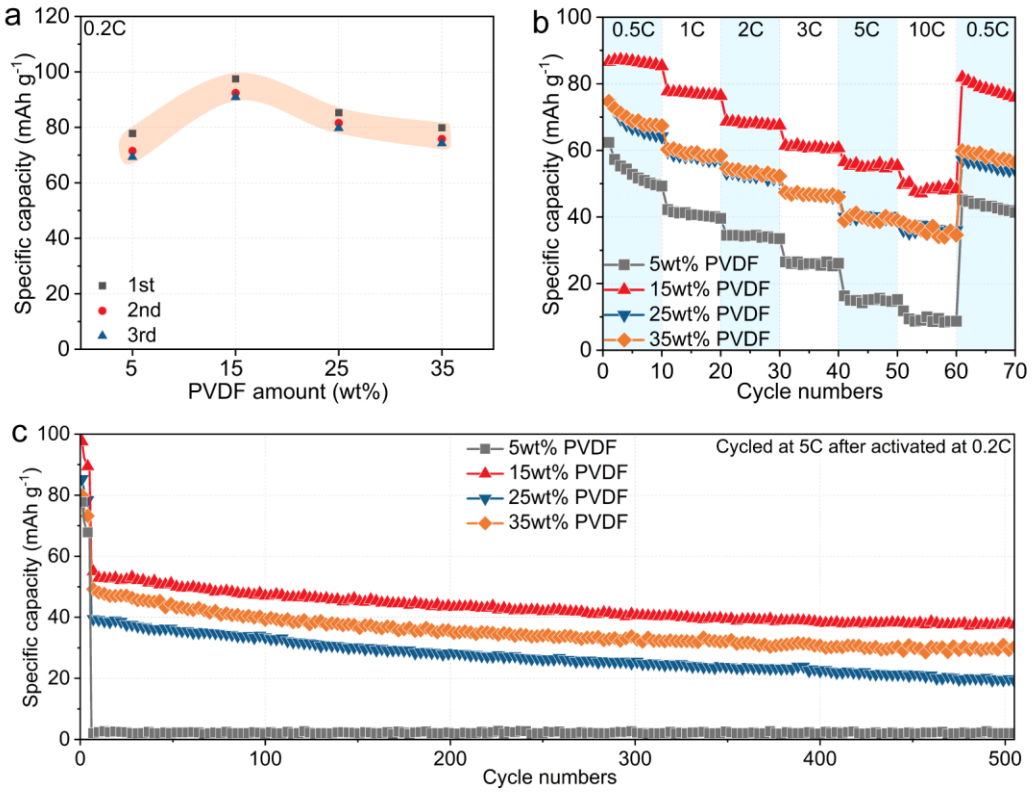

Fig. S39. (a) Plots of carbon content of KVPF-15wt% PVDF and KVPF-25wt% PVDF. (b) Galvanostatic charging/discharging profiles of KVPF-25wt% PVDF. (b) Rate capability. (c) Long-term cyclability at 5C.

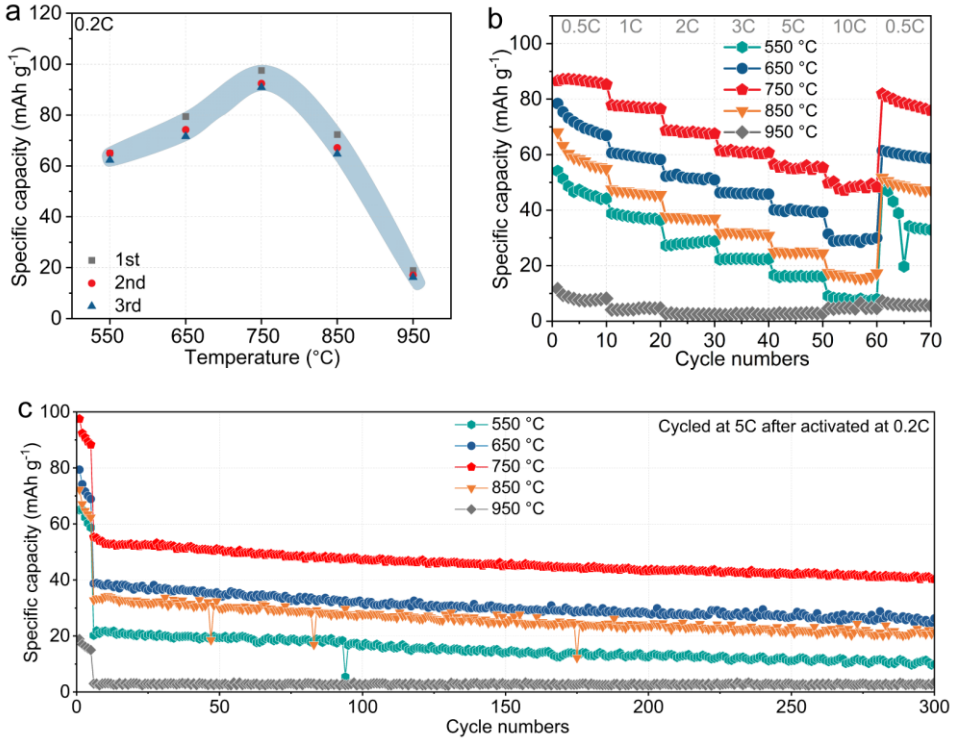

Fig. S40. (a) Illustration comparison practical capacities of KVPF-PVDF at different calcination temperatures. (b) Rate capability. (c) Long-term cyclability at 5C.

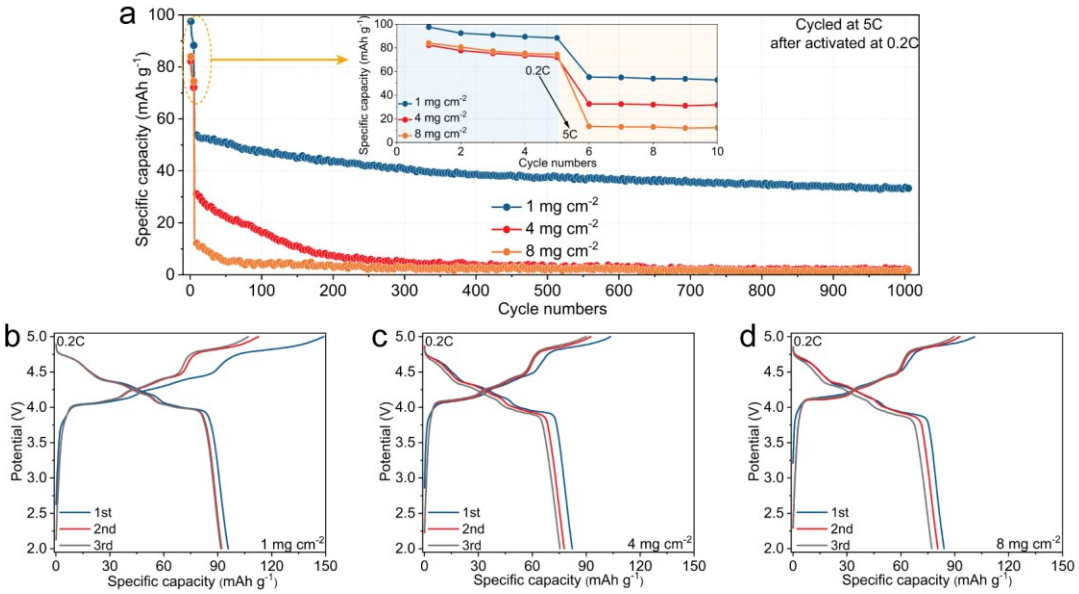

Fig. S41. (a) Long-term cyclability of KVPF-PVDF with different loading. (b, c, d) Galvanostatic charging/discharging profiles of KVPF-PVDF at 0.2C with different loading.

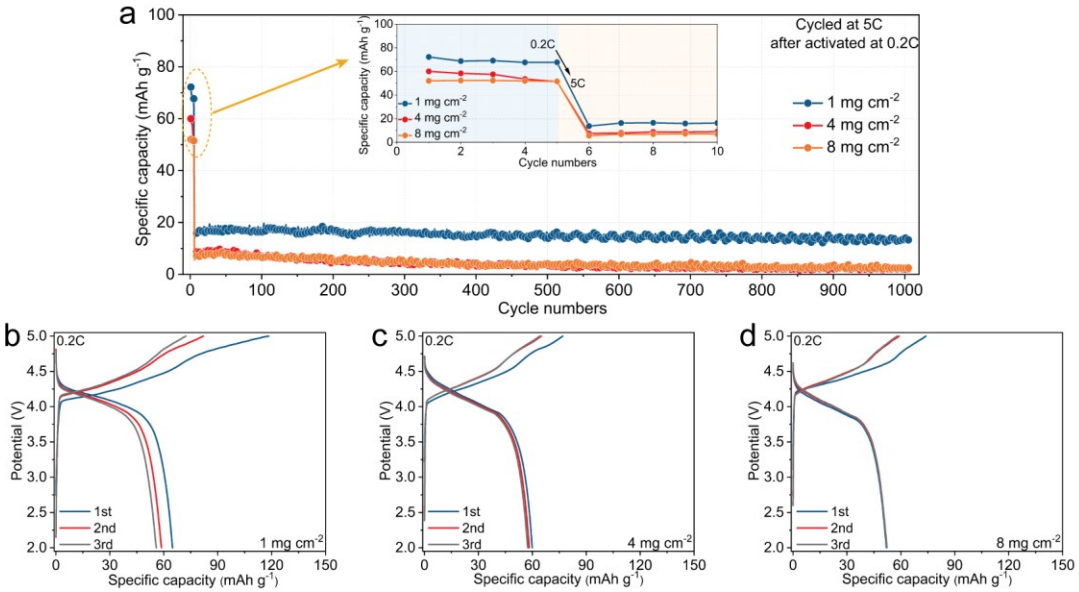

Fig. S42. (a) Long-term cyclability of KVPF-PTFE with different loading. (b, c, d) Galvanostatic charging/discharging profiles of KVPF-PTFE at 0.2C with different loading.

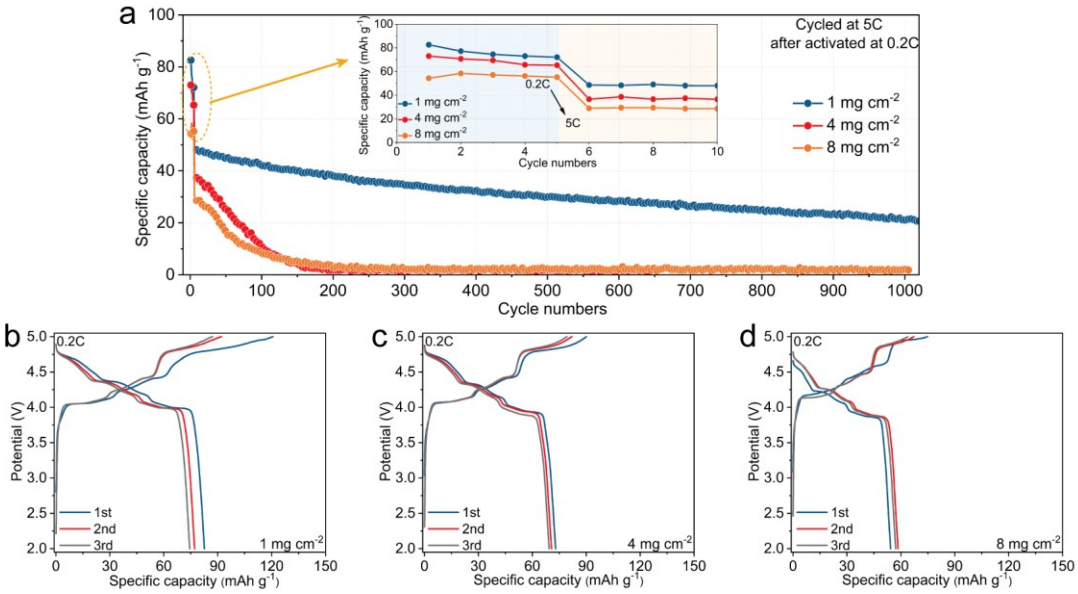

Fig. S43. (a) Long-term cyclability of KVPF-CTR with different loading. (b, c, d) Galvanostatic charging/discharging profiles of KVPF-CTR at 0.2C with different loading.

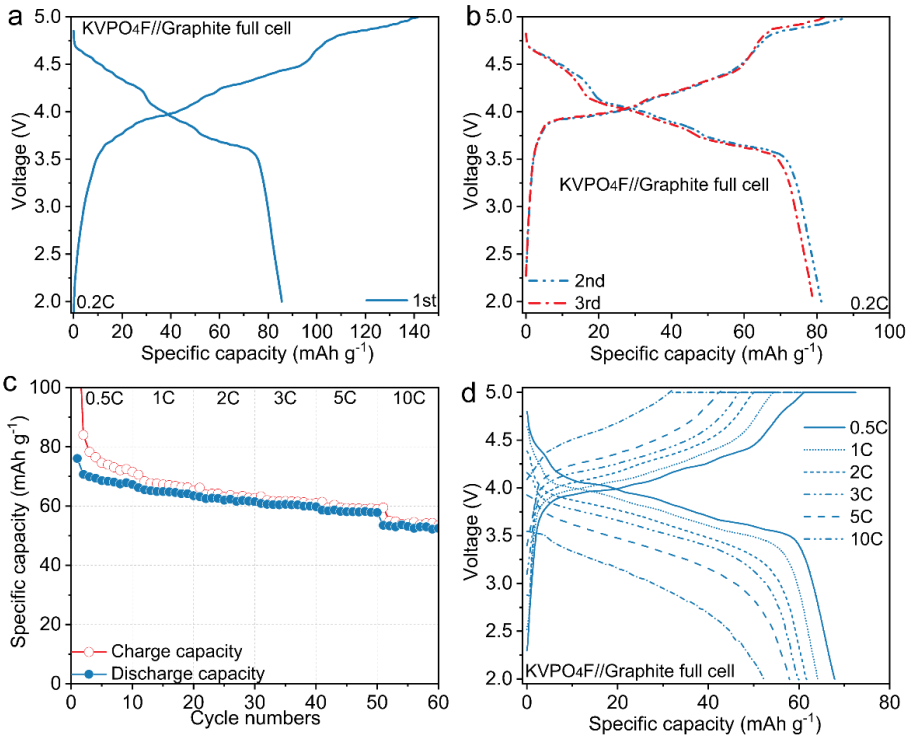

Fig. S44. (a, b) Galvanostatic charge-discharge curves at 0.2C and (c, d) Rate capability of KVPF-PVDF//graphite full-cell. For the KVPF-PVDF//graphite coin full-cell, the cathode/anode area is 1.54 cm^2, the cathode active material loading mass is 3.0 mg, the anode active material loading mass is 1 mg, the negative-to-positive (N/P) ratio is 1.1, and the nominal capacity is 0.25 mAh.

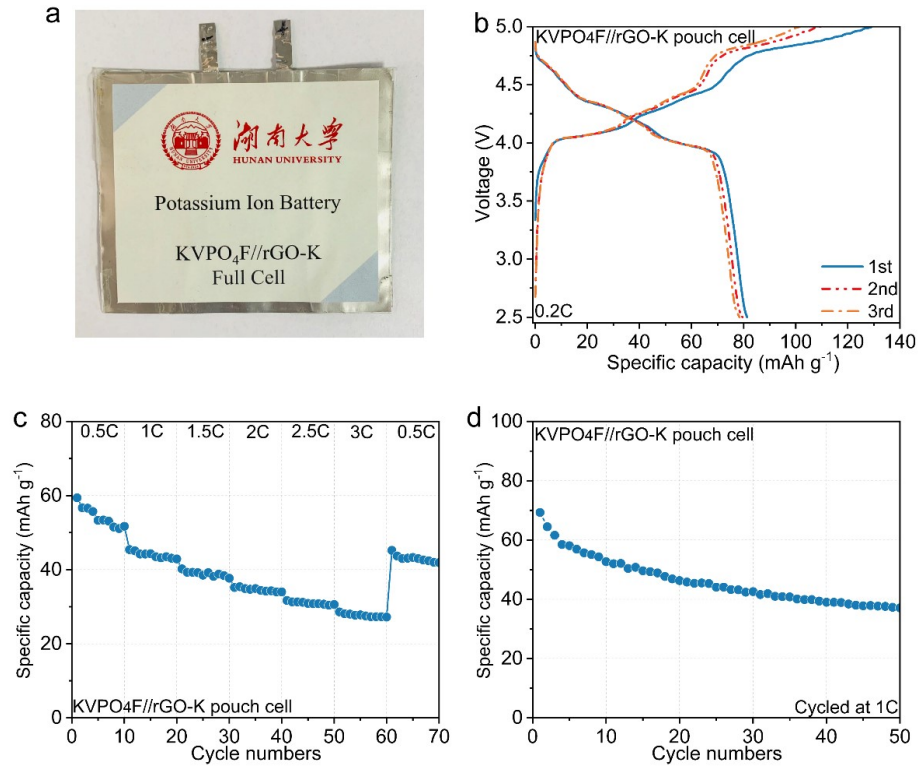

Fig. S45. (a) Digital pictures of the $KVPO_4F$//rGO-K pouch cell. (b) Charging/discharging curves of $KVPO_4F$//rGO-K pouch cell. (c) Rate capability and (d) cycle performance at 1C of $KVPO_4F$//rGO-K pouch cell. The pouch $KVPO_4F$//rGO-K full-cells were assembled by pairing our KVPF-PVDF cathodes with rGO-modified metallic potassium anodes.[7] For the $KVPO_4F$//rGO-K pouch cell, the cathode/anode area is 20 cm^2, the cathode active material loading mass is 14 mg, the anode active material is 50 μm thick rGO-modified metallic potassium (theoretical areal capacity of rGO-K anode is about 2.95 mAh cm^{-2}), the negative-to-positive (N/P) ratio is ~44, and the nominal capacity is 1 mAh.

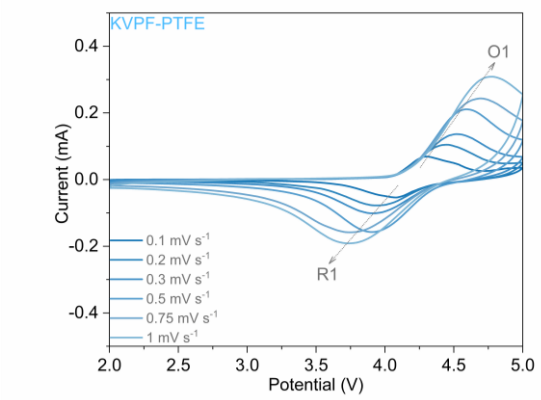

Fig. S46. CV curves of KVPF-PTFE at various scan rates.

Supplementary Note 9:

The K^+ ion diffusion coefficient (D_K) is calculated by using the Randles–Sevcik equation (**Eq. S9**):[8]

$$I_P = 2.69 \times 10^5 \times n^{\frac{3}{2}} A D_k^{\frac{1}{2}} C v^{\frac{1}{2}} \quad \textbf{(Eq. 9)}$$

where I_P is the peak current, n is the number of transferred electrons, A is the surface area of the electrode, C is the K-ion concentration inside the electrode, and v is the scan rate. As displayed in **Fig. S47c-f**, the peak current exhibits a good linear relationship with $v^{\frac{1}{2}}$ for all redox couple peaks.

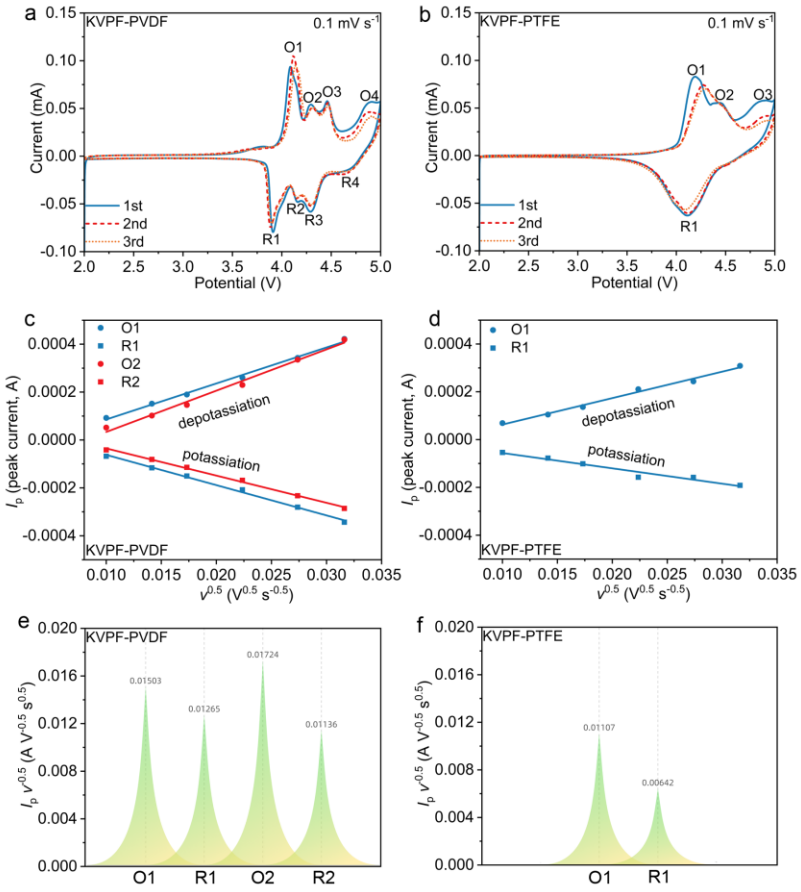

Fig. S47. (a, b) CV measurements of the KVPF-PVDF and KVPF-PTFE electrode at 0.1 mV s^{-1}. (c, d) Linear fitting for the peak current (I_P) versus the square root of scan rate ($v^{1/2}$) collected from CV profiles. (e, f) The calculated $I_P v^{1/2}$ values.

Supplementary Note 10:

The accurate determination of R_{ct} and R_{SEI} values is important but typically difficult without extra information of the reactions. Introducing a physical model to fit the EIS data is not employed because it may impose subjectivity to the results. Recently, the distribution of relaxation time (DRT) technique has been developed to separate different polarization processes, which is obtained by transforming the EIS data from frequency domain to time domain, thus is considered as a powerful means of displaying immittance data and can accurately distinguish the highly overlapped physical and chemical processes.[9] **Fig. S48** shows the typical DRTs results of corresponding impedance curves of KVPF-PVDF, KVPF-CTR and KVPF-PTFE. The X-axis is time constant, and the peak area represents the impedance related process. Therefore, various processes with different time constant can be separated and identified in the DRT diagram.

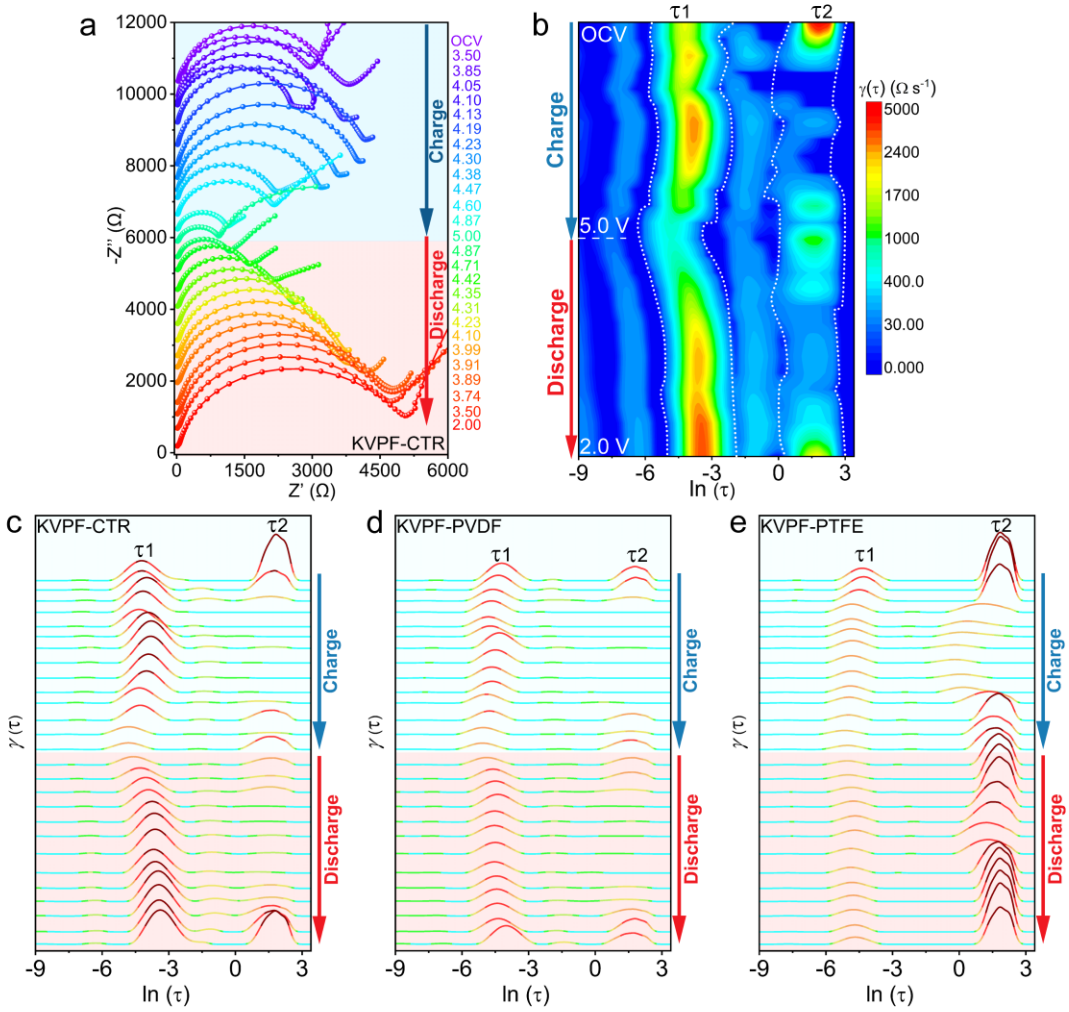

Fig. S48. (a) *In-situ* EIS Nyquist plots and (b, c) corresponding DRTs of KVPF-CTR. The DRTs plot of (d) KVPF-PVDF and (e) KVPF-PTFE electrode.

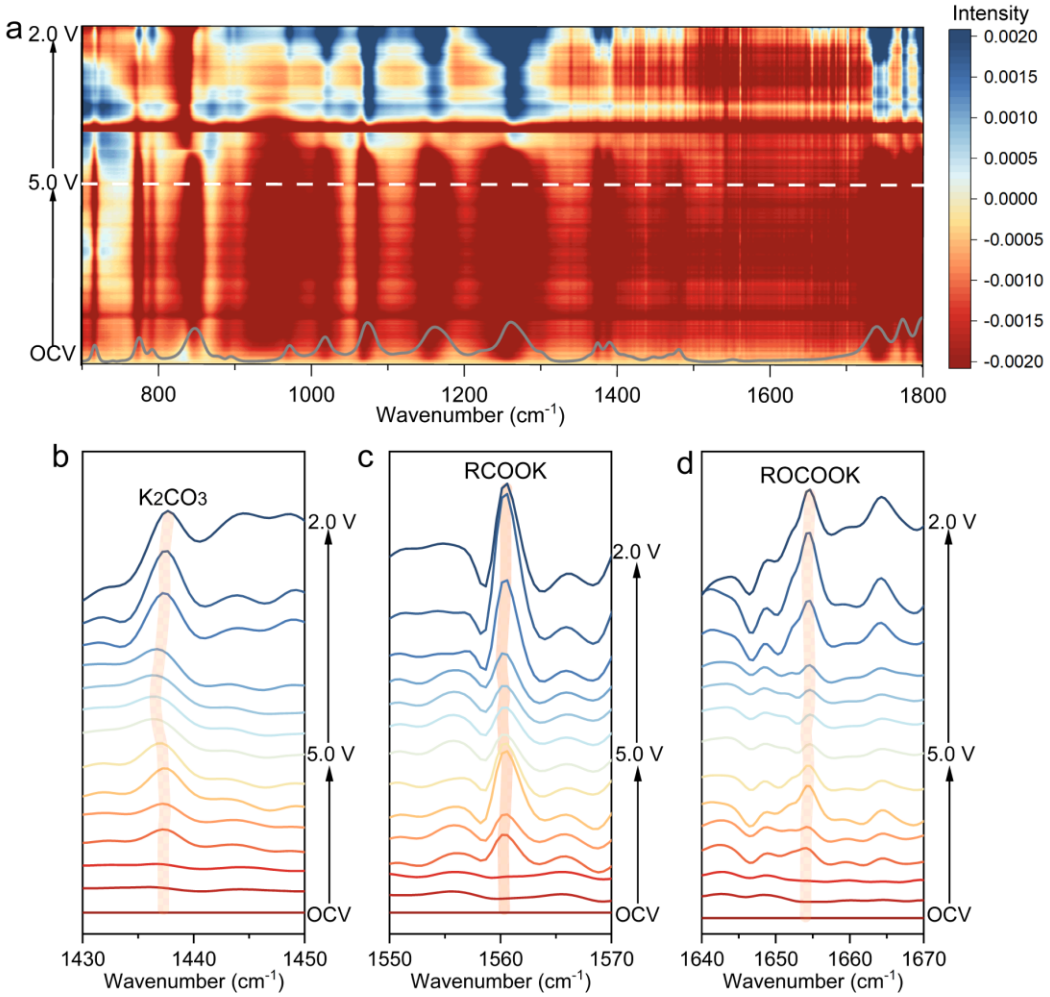

Fig. S49. Dynamic evolution of CEI derived from electrolytes on KVPF-PVDF cathode during electrochemical operations captured by *in-situ* FTIR.

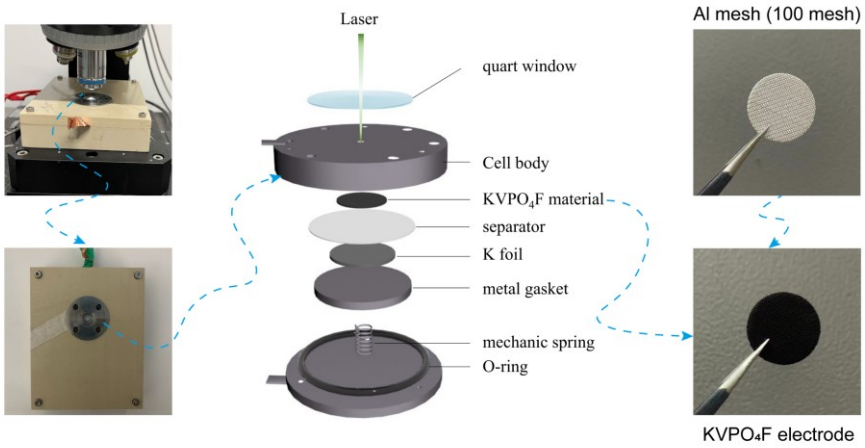

Fig. S50. Schematic sketch of *in-situ* Raman cell.

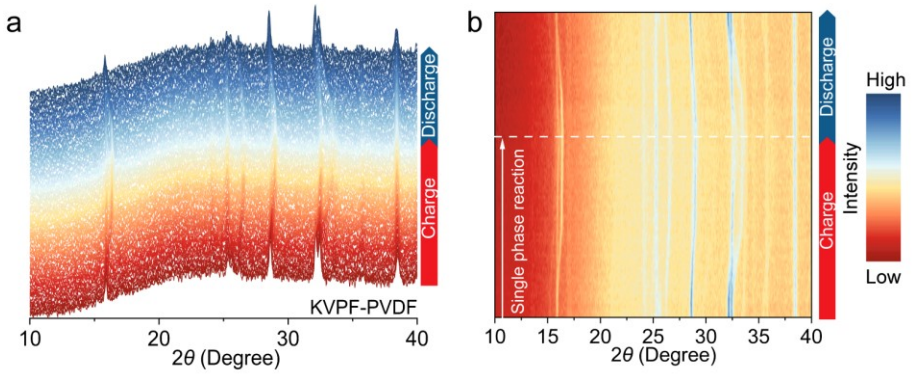

Fig. S51. *In-situ* XRD patterns of KVPF-PVDF.

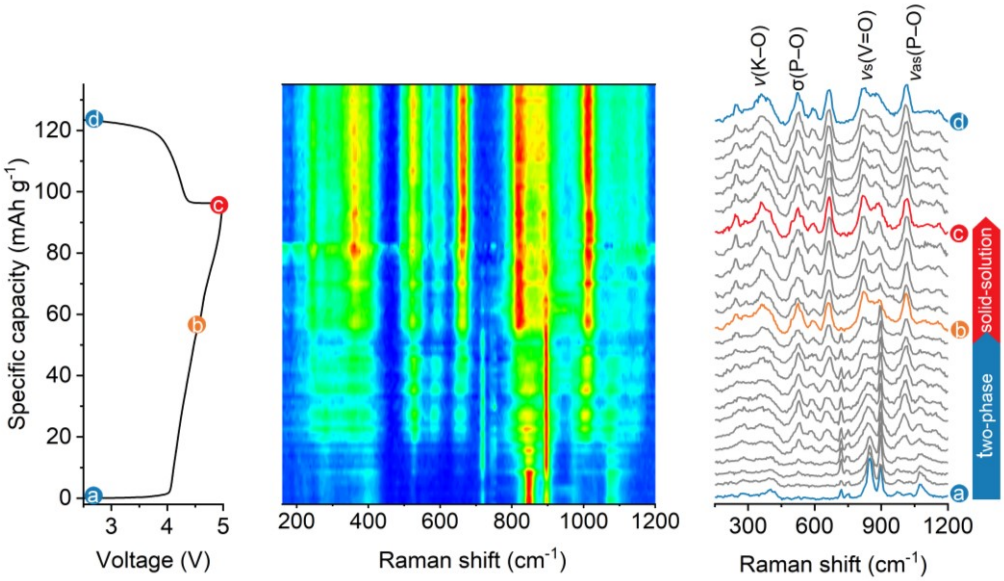

Fig. S52. The *in-situ* Raman test of KVPF-PTFE.

Table S1. Fractional atomic parameters of KVPF-PTFE with $Pna2_1$ space group.

Atom	Occupancy	Site	*x*	*y*	*z*	U_{iso}
K1	0.5	4a	0.3879	0.7877	0.2834	0.0158
K1'	0.5	4a	0.3799	0.7821	0.3304	0.0099
K2	0.5	4a	0.1015	0.6654	-0.0149	0.0677
K2'	0.5	4a	0.1023	0.7166	0.0834	0.0094
V1	1	4a	0.3834	0.4998	-0.0004	0.0316
V2	1	4a	0.2453	0.2641	0.2499	0.0271
P1	1	4a	0.4979	0.3147	0.2412	0.0225
P2	1	4a	0.1798	0.4982	0.5052	0.0226
O1	1	4a	0.4694	0.4866	0.1293	0.0053
O2	1	4a	0.5094	0.4676	0.3705	0.0056
O3	1	4a	0.3929	0.2178	0.2820	0.0043
O4	1	4a	0.5954	0.2092	0.2339	0.0026
O5	1	4a	0.0979	0.3361	0.5224	0.0092
O6	1	4a	0.1180	0.6775	0.4637	0.0015
O7	1	4a	0.2585	0.5272	0.6339	0.0019
O8	1	4a	0.2886	0.4779	0.4310	0.0293
O9/F1	1	4a	0.2883	0.5450	0.8959	0.0104
O10/F2	1	4a	0.2470	0.4644	0.1190	0.0107

Table S2. Fractional atomic parameters of KVPF-PVDF with $Pna2_1$ space group.

Atom	Occupancy	Site	*x*	*y*	*z*	U_{iso}
K1	0.5	4a	0.3769	0.7666	0.2939	0.0103
K1'	0.5	4a	0.3977	0.7760	0.3141	0.0103
K2	0.5	4a	0.0998	0.6839	0.0451	0.0103
K2'	0.5	4a	0.1052	0.7051	0.0895	0.0103
V1	1	4a	0.3854	0.4952	0.0038	0.0213
V2	1	4a	0.2514	0.2550	0.2531	0.0118
P1	1	4a	0.5023	0.3182	0.2423	0.0100
P2	1	4a	0.1837	0.5104	0.5063	0.0100
O1	1	4a	0.5008	0.4665	0.1398	0.0100
O2	1	4a	0.5204	0.5138	0.3618	0.0100
O3	1	4a	0.3904	0.2114	0.2911	0.0100
O4	1	4a	0.5734	0.1777	0.2367	0.0100
O5	1	4a	0.1061	0.3196	0.5411	0.0100
O6	1	4a	0.1190	0.6776	0.4797	0.0100
O7	1	4a	0.2645	0.5544	0.6159	0.0100
O8	1	4a	0.2450	0.4751	0.3741	0.0100
F1	1	4a	0.2632	0.5316	0.8919	0.0100
F2	1	4a	0.2690	0.5134	0.1478	0.0100

Table S3. Selected interatomic distances of KVPF-PTFE and KVPF-PVDF.

Bond	Distance for KVPF-PTFE (Å)	Bond	Distance for KVPF-PVDF (Å)
V1-O1	1.7548	V1-O1	2.0753
V1-O2	1.9396	V1-O2	1.9318
V1-O5	2.1689	V1-O5	2.1166
V1-O6	2.0872	V1-O6	2.0493
V1-X1*	1.6567	V1-F1	1.9792
V1-X2*	2.1597	V1-F2	2.1384
V2-O3	1.9387	V2-O3	1.8491
V2-O4	1.9291	V2-O4	2.3295
V2-O7	1.9412	V2-O7	1.9511
V2-O8	2.4078	V2-O8	1.9077
V2-X1*	2.1204	V2- F1	2.0607
V2-X2*	1.8779	V2- F2	2.0085

*X could be O or F.

Table S4. Comparison of electrochemical performance reported for $KVPO_4F$.

Material	Specific capacity (mAh g^{-1})	Rate capacity (mAh g^{-1})	Cycling stability	Working voltage (V)	Electrolyte	Ref.
KVPF-PVDF	95.8 (26.2 mA g^{-1})	48.3 (1.31 A g^{-1})	64.5% (1000th, 0.655 A g^{-1})	4.02	0.8M KPF_6 in EC/DEC+1.5wt%TMSP	This work
$KVPO_4F_{0.5}O_{0.5}@C_2H_2$	84 (26.2 mA g^{-1})	48.1 (1.31 A g^{-1})	88% (20th, 0.0262 A g^{-1})	4.2	0.8M KPF_6 in EC/DEC	10
$KVPO_4F_{0.5}O_{0.5}$	84 (26.2 mA g^{-1})	Failed (1.31 A g^{-1})	Not provided	Not provided		
KVPF-Al	73.3 (26.2 mA g^{-1})	33.6 (1.31 A g^{-1})	41.5% (1000th, 0.655 A g^{-1})	4.01	0.8M KPF_6 in EC/DEC+1.5wt%TMSP	11
KVPF-film	92.4 (26.2 mA g^{-1})	49.0 (1.31 A g^{-1})	74.9% (1000th, 0.655 A g^{-1})	4.02		
$KVPO_4F$	70 (6.65 mA g^{-1})	67.0 (0.655 A g^{-1})	97% (30th, 0.0066 A g^{-1})	4.0	0.7M KPF_6 in EC/DEC	2
$KVPO_4F$	105 (5 mA g^{-1})	44.0 (0.3 A g^{-1})	78.3% (10th, 0.02 A g^{-1})	4.0	0.7M KPF_6 in EC/DEC	4
$KVPO_{4.36}F_{0.64}$	85 (5 mA g^{-1})	54.0 (0.3 A g^{-1})	91.7% (10th, 0.02 A g^{-1})	Not provided		
KVPF@C-bulk	94.2 (20 mA g^{-1})	21.2 (0.655 A g^{-1})	88.1% (200th, 0.0655 A g^{-1})	4.12	1M KPF_6 in PC/EC	12
KVPF@C-PMS	101.5 (20 mA g^{-1})	70.1 (0.655 A g^{-1})	85.1% (200th, 0.0655 A g^{-1})	4.02		
KVPF	98.6 (20 mA g^{-1})	Failed (0.5 A g^{-1})	71.0% (55th, 0.05 A g^{-1})	4.03	0.8M KPF_6 in EC/DEC	13
KVPF@3DC	103 (20 mA g^{-1})	60.2 (0.5 A g^{-1})	85.4% (550th, 0.5 A g^{-1})	4.03		
KVPF@C-bare	95 (20 mA g^{-1})	88.8 (0.05 A g^{-1})	84.9% (50th, 0.05 A g^{-1})	4.03	0.8M KPF_6 in EC/DEC	5
KVPF@C-MC2	100 (20 mA g^{-1})	84.4 (0.05 A g^{-1})	100% (50th, 0.05 A g^{-1})	4.03		
KVPF@C	82.9 (25 mA g^{-1})	46.3 (1 A g^{-1})	Not provided	Not provided	1M KPF_6 in PC/EC	14
KVPF@K	101.6 (25 mA g^{-1})	47.9 (1 A g^{-1})	53.2% (100th, 0.2 A g^{-1})	3.96		
KVPF@KCO-K	142 (25 mA g^{-1})	70.6 (1 A g^{-1})	74.1% (100th, 0.2 A g^{-1})	3.98		
KVPF-ball	105 (20 mA g^{-1})	59.2 (5 A g^{-1})*	65% (100th, 0.02 A g^{-1})	4.10	0.5M KPF_6 in PC/FEC	15
KVPF-platelet	94 (20 mA g^{-1})	30.0 (5 A g^{-1})*	53% (100th, 0.02 A g^{-1})	4.01		
KVPF-flower	103 (20 mA g^{-1})	87.6 (5 A g^{-1})*	80% (900th, 1 A g^{-1})	3.97		
KVPF-CTR	74.6 (26.2 mA g^{-1})	46.2 (2.62 A g^{-1})**	80.2% (100th, 0.0655 A g^{-1})	4.00	1M KPF_6 in PC/EC+5vol%FEC	16
KVPF@CMK-3	103.2 (26.2 mA g^{-1})	90.1 (2.62 A g^{-1})**	88.2% (500th, 1.31 A g^{-1})	3.93		
KVPF-CTR	94.2 (20 mA g^{-1})	Failed (10 A g^{-1})***	73.5% (100th, 0.05 A g^{-1})	3.96	1M KPF_6 in PC/EC+5wt%FEC	17
KVPF-P3/C	106.5 (20 mA g^{-1})	73.8 (10 A g^{-1})***	82.5% (1000th, 1 A g^{-1})	3.97		
KVPF@rGO	103.2 (20 mA g^{-1})	88.1 (5 A g^{-1}))****	76.9% (500th, 1.31 A g^{-1})	3.94	1M KPF_6 in PC/EC+5vol%FEC	18
KVPF	85.0 (20 mA g^{-1})	26.8 (5 A g^{-1}))****	23.3% (500th, 1.31 A g^{-1})	3.95		

Note: The test methods for rate performance and cycle stability of some papers are slow charge and fast discharge mode (marked with "*") rather than standard constant current charge/discharge mode, no doubt this will be significant improvement in electrochemical performance.

*The rate performance is 50 mA g^{-1} for charge and 5 A g^{-1} for discharge (slow charging and fast discharging mode). The cycling stability test with a fixed current density of 0.02A g^{-1}.

**The condition of rate performance for KVPF@CMK-3 is 65.5 mA g^{-1} for charge and 1.31 A g^{-1} for discharge (slow charging and fast discharging mode). The condition of cycling stability is not clear.

***The condition of rate performance for KVPF@P3/C is 65.5 mA g^{-1} for charge and 1 A g^{-1} for discharge (slow charging and fast discharging mode). The condition of cycling stability is not clear.

****The condition of rate performance for KVPF@RGO is 65.5 mA g^{-1} for charge and 1.31 A g^{-1} for discharge (slow charging and fast discharging mode). The condition of cycling stability is not clear.

Notes and references

1. Chen, Z.C. et al. One-step Method of Carbon Thermal Reduction and Nitride to Produce Vanadium Nitrogen Alloy. *Advanced Materials Research* **476**, 194-198 (2012).
2. Chihara, K., Katogi, A., Kubota, K. & Komaba, S. $KVPO_4F$ and $KVOPO_4$ toward 4 volt-class potassium-ion batteries. *Chemical Communications* **53**, 5208-5211 (2017).
3. Fedotov, S.S. et al. $AVPO_4F$ (A= Li, K): a 4 V cathode material for high-power rechargeable batteries. *Chemistry of Materials* **28**, 411-415 (2016).
4. Kim, H. et al. A New Strategy for High-Voltage Cathodes for K-Ion Batteries: Stoichiometric $KVPO_4F$. *Advanced Energy Materials* **8**, 1801591 (2018).
5. He, X.D., Zhang, L.M., Jiang, C.H. & Chen, C.H. Elevating cyclability of an advanced $KVPO_4F$ cathode via multi-component coating strategy for high-performance potassium-ion batteries. *Chemical Engineering Journal* **433**, 134634 (2022).
6. Kim, H., Tian, Y. & Ceder, G. Origin of Capacity Degradation of High-Voltage $KVPO_4F$ Cathode. *Journal of the Electrochemical Society* **167**, 110555 (2020).
7. Wu, J.F. et al. Building K-C Anode with Ultrahigh Self-Diffusion Coefficient for Solid State Potassium Metal Batteries Operating at -20 to 120 °C. *Advanced Materials* **35**, 2209833 (2023).
8. Zanello, P., Nervi, C. & De Biani, F.F. Inorganic electrochemistry: theory, practice and application, (Royal Society of Chemistry, 2019).
9. Lu, Y., Zhao, C.Z., Huang, J.Q. & Zhang, Q. The timescale identification decoupling complicated kinetic processes in lithium batteries. *Joule* **6**, 1172-1198 (2022).
10. Larbi, L. et al. Enhanced Performance of $KVPO_4F_{0.5}O_{0.5}$ in Potassium Batteries by Carbon Coating Interfaces. *ACS Applied Materials & Interfaces* **15**, 18992-19001 (2023).
11. Fu, Q. et al. Regulating cathode surface hydroxyl chemistry enables superior potassium storage. *Proceedings of the National Academy of Sciences of the United States of America* **120**, e2301622120 (2023).
12. Xie, C. et al. Pomegranate-Like $KVPO_4F$@C Microspheres as High-Volumetric-Energy-Density Cathode for Potassium-Ion Batteries. *Small* **18**, 2204348 (2022).
13. Liu, Z.M., Wang, J. & Lu, B.A. Plum pudding model inspired $KVPO_4F$@3DC as high-voltage and hyperstable cathode for potassium ion batteries. *Science Bulletin* **65**, 1242-1251 (2020).
14. Heng, Y.L. et al. Low-Strain and High-Energy $KVPO_4F$ Cathode with Multifunctional Stabilizer for Advanced Potassium-Ion Batteries. *Energy & Environmental Materials*, e12721.
15. Liao, J.Y. et al. A long lifespan potassium-ion full battery based on $KVPO_4F$ cathode and VPO_4 anode. *Journal of Power Sources* **451**, 227739 (2020).
16. Xu, J. et al. $KVPO_4F$/carbon nanocomposite with highly accessible active sites and robust chemical bonds for advanced potassium-ion batteries. *Green Energy & Environment* **8**, 1469-1478 (2023).
17. Liao, J. et al. Synthesis of $KVPO_4F$/Carbon Porous Single Crystalline Nanoplates for High-Rate Potassium-Ion Batteries. *Nano Letters* **22**, 4933-4940 (2022).
18. Xu, J. et al. Facile synthesis of $KVPO_4F$/reduced graphene oxide hybrid as a high-performance cathode material for potassium-ion batteries. *Journal of Energy Chemistry* **68**, 284-292 (2022).